RESEARCH ARTICLE

Continuous estimation of coseismic and early postseismic slip phenomena via the GNSS carrier phase to fault slip approach: a case study of the 2011 Tohoku-Oki sequence

Yusuke Tanaka[1*] , Yusaku Ohta[2,3,4] and Shin'ichi Miyazaki[5]

Abstract

The transition process from coseismic to early postseismic phenomena within a half-day remains a significant topic for understanding the slip budget and friction properties of the fault. However, the investigation of this phase has undergone limited advancement. This is mainly due to the lack of precision pertaining to the Global Navigation Satellite System (GNSS) analysis caused by difficulty of separation between fault slip and other unknown parameters such as tropospheric delay. Therefore, we propose an alternative approach (phase-to-slip; PTS) that detects fault slip directly from GNSS carrier phase variation without conventional positioning. Since the PTS simultaneously estimates fault slip and other unknowns, we can quantitatively evaluate their separation accuracy and contribution in the estimation. This study attempts to continuously estimate the coseismic and early postseismic slip of the 2011 Tohoku-Oki sequence using the PTS method. We analyzed 1-Hz carrier phase data for approximately 2 h before and after the mainshock origin (2011/03/11/05:46UTC). As a result, we successfully obtained the coseismic slip of the M_W9.0 mainshock and two major aftershocks in the off-Ibaraki (M_W7.8) and off Iwate (M_W7.4) regions. For all three events, the estimated slip distribution, equivalent moment magnitude, and calculated displacement field well agreed with those from the conventional positioning. Additionally, our results suggest postseismic slip mainly in the downdip area adjacent to the mainshock rupture. We obtained three major slip areas around the downdip region near Aomori, Iwate, and Miyagi. The estimated slip amount reaches approximately 0.1–0.2 m in 34 min immediately after the mainshock. The equivalent seismic moment of the slip areas near Iwate and Miyagi were approximately M_W7.4. This amount is similar or slightly greater than the estimations based on conventional positioning. Significant overlap is observed in the locations of the slip areas. In this manner, PTS continuously detected a series of coseismic and early postseismic slips with timescale ranging from a few minutes to an hour. Our results demonstrate the capability of the PTS method for broadband fault slip monitoring and its potential contribution to the investigation of early postseismic phenomena.

Keywords: GNSS carrier phase, Early postseismic, Half-day, Fault slip monitoring

1 Introduction

The cycle of earthquake occurrences results in fault slip with an extensive range of timescales, from dynamic rupture propagation within seconds or minutes, to afterslip and interseismic coupling ranging for more than few years or decades. To understand the entire process of

*Correspondence: yusuke.tanaka.d8@tohoku.ac.jp

[1] Solid Earth Physics Laboratory, Graduate School of Science, Tohoku University, 6-3 Aza-Aoba, Aramaki, Aoba-ku, Sendai 980-8578, Japan
Full list of author information is available at the end of the article

strain accumulation and slip budget over one cycle of an earthquake, it is necessary to accurately detect the broadband fault slip or deformation phenomena. To achieve this goal, the traditional GNSS analysis is implemented for broadband applications. For example, high-rate kinematic positioning time series have been utilized to detect seismic waves (e.g., Hirahara et al. 1994; Hatanaka et al. 1996; Larson et al. 2003; Bock et al. 2004; Ohta et al. 2006). Larson et al. (2003) and Bock et al. (2004) captured surface waves generated by the 2002 Denali earthquake using a 1 Hz GNSS time series. Furthermore, previous studies (e.g., Yokota et al. 2009; Miyazaki et al. 2004) also estimated the dynamic rupture process using the ground motion obtained from kinematic GNSS. For example, Miyazaki et al. (2004) inverted the spatiotemporal development of the coseismic slip distribution of the 2003 Tokachi-Oki earthquake. These studies successfully demonstrated that GNSS can be used as a seismometer. Real-time magnitude estimation based on the coseismic displacement detected by kinematic GNSS has also been achieved in several studies (e.g., Blewitt et al. 2006, 2009; Larson 2009; Allen and Ziv 2011; Colosimo et al. 2011; Ohta et al. 2012, 2015; Melgar et al. 2012, 2013; Melgar and Bock 2013; Minson et al. 2013). Blewitt et al. (2006, 2009) described the basic concept of applying such rapid source estimation to tsunami warnings. Ohta et al. (2012) demonstrated real-time source estimation based on GNSS for precise tsunami forecasting through a case study of the 2011 Tohoku-Oki earthquake. These studies proposed the availability of GNSS for early earthquake and tsunami warnings.

In contrast, daily precise static positioning time series have been used in several studies pertaining to slip phenomena with longer timescales, such as afterslip (e.g., Bürgmann et al. 1997, 2002; Freed et al. 2006; Ozawa et al. 2011; Barnhart et al. 2016), slow slip events (e.g., Hirose et al. 1999; Ozawa et al. 2002; Nishimura et al. 2013), and interseismic coupling (e.g., Ito et al. 2000; Suwa et al. 2006; Nishimura et al. 2018). For example, Ozawa et al. (2011) estimated the afterslip distribution in the first two weeks after the 2011 Tohoku-Oki earthquake. Such studies have remarkably expanded our knowledge regarding the various modes of stress accumulation and release on plate boundaries. As described above, traditional GNSS analysis establishes acceptable performance for a timescale within a few minutes and beyond half a day.

However, the traditional GNSS analysis exhibits a few problems for intermediate timescales ranging from a few minutes to half a day. Due to the difficulty in separating the displacement of the GNSS antenna and other unknown parameters such as tropospheric delay during GNSS analysis, the precision of the time series will deteriorate in such a time window. The available GNSS analysis

software simultaneously estimates the time dependence of the wet zenith tropospheric delay with the coordinate time series. Hirata and Ohta (2016) investigated the impact of process noise optimization on kinematic GNSS site coordinate time series. They inferred that with the use of optimized process noise, the standard deviation of the coordinate time series could be reduced by approximately 15% in the horizontal component and 30% in the vertical component.

However, it is challenging to optimize these process noises for each observation site. Thus, the kinematic GNSS time series can be significantly affected by process noise values that are not fully optimized and other noise sources, such as multipath errors. Thus, very few studies exist which utilizes GNSS for this timescale. One of the most essential phenomena in these time bands is the occurrence of afterslip immediately after a large earthquake.

The early afterslip probably occupies a significant fraction of the total slip budget of the earthquake cycle. Langbein et al. (2006) compared the coseismic displacement amount and equivalent moment magnitude obtained from daily time series and kinematic time series. Further, they demonstrated that the two estimations differed by more than 10% to 30%. In other words, moment release by early afterslip within a half-day is expected to reach more than several tens of percent of the coseismic moment. Furthermore, the early postseismic phase may be essential for understanding the friction law of faults. Several researchers have presented a theoretical explanation of the temporal evolution of afterslip with various friction models, such as rate-and-state, rate-dependent with steady state, and Omori law. A few of them (e.g., Wennerberg and Sharp 1997; Perfettini and Ampuero 2008; Helmstetter and Shaw 2009) pointed out that the early phase within a day or two days exhibits the most considerable discrepancy between assumed friction laws, and the latter phase can usually be fitted by both models. Therefore, a lack of resolution for minutes to half a day causes profound misunderstanding in both the slip budget and its controlling physics. Although several previous studies analyzed the early postseismic phase within a half-day based on GNSS (Miyazaki and Larson 2008; Munekane 2012; Mitsui and Heki 2013; Malservisi et al. 2015; Twardzik et al. 2019); Tsang et al. 2019), the number of such studies is small compared to that of studies on other time periods such as coseismic and more prolonged postseismic deformation. Additionally, only few of them attempted to estimate the temporal evolution of the early afterslip. Others estimated the total amount for a certain period. Continuous estimation of the transition process from coseismic to early postseismic phases is still unprecedented with sufficient temporal resolution.

Tanaka *et al. Progress in Earth and Planetary Science* (2022) 9:55

Page 3 of 20

Here, we focused on a method that directly links the GNSS carrier phase change to fault slip, instead of the conventional method of estimating the time dependence of the fault slip from the coordinate time series. As the conventional positioning analysis is originally independent of the controlling physics of deformation and its source, we cannot simultaneously investigate the contribution of fault slip and other error factors. Once we obtain the coordinate time series, the contribution of other factors is fixed as the noise pertaining to the time series. This is an obstacle toward improving the accuracy of the separation between the fault slip and other errors. Several previously conducted studies have directly used GNSS carrier phase variations as observable. Point precise Variance Detection (PVD) developed by Issiki et al. (2000) and VADASE (Variometric Approach for Displacements Analysis Stand-alone Engine) proposed by Colosimo et al. (2011) are pioneering methods for detecting short-term relative movements of GNSS receivers, especially within a few minutes, from carrier phase variations. These studies suggested the possibility of a low-cost and straightforward approach based on single receiver and raw carrier phase data, which still displayed an accuracy comparable to that of conventional positioning. Cervelli et al. (2002) proposed a method of inverting fault slip directly from carrier phase variations (hereafter referred to as phase-to-slip (PTS)). This method relates carrier phase and fault slip via Green's function and geometric translation from movement along the surface (e.g., EW-NS-UD) to that along the line of sight toward GNSS satellites.

Furthermore, the PTS simultaneously estimates the temporal evolution of fault slip, tropospheric delay, and phase ambiguity from Kalman filtering. The developed method was applied to aseismic fault slip on the south flank of the Kilauea volcano, Hawaii. They successfully detected a fault slip of only a few centimeters within one day, with a time resolution of 30 s. Tanaka et al. (2019) attempted its application to coseismic slip within a timescale of a few minutes. They estimated the slip distribution of the 2016 Kumamoto earthquake (M_w7.0) and obtained results consistent with conventional positioning. They successfully demonstrated the applicability of PTS for precise and robust seismic monitoring. The PTS directly estimates the fault slip from the carrier phase change without conventional coordinate time series estimation. It may be advantageous to interpret the trade-off between unknown parameters, such as fault slip and tropospheric delay.

In this study, we evaluated the ability of PTS based on the application of the 2011 Tohoku-Oki earthquake (M_w9.0) sequence. Furthermore, we demonstrated that the PTS can be applied not only to coseismic slip but also to the time dependence of the major aftershocks and early afterslip just after the mainshock. We also quantitatively investigated the trade-off between fault slip and other unknown parameters during the PTS analysis. Finally, we discuss the capability of PTS for broadband fault slip monitoring and its future prospects.

2 Methods and analysis

Here, we describe the principles of the PTS method based on Cervelli et al. (2002) and Tanaka et al. (2019), together with the explanations about its application to the 2011 Tohoku-Oki sequence. See also the PTS flowchart shown in Additional file 2: Figure S1.

2.1 Input of the PTS and analysis period

Input data of the PTS are carrier phase and satellite orbit. We used 1-Hz carrier phase data of continuous GNSS sites established by the Geospatial Information Authority of Japan, named GEONET (GNSS Earth Observation Network). The Global Positioning Satellite (GPS) system was solely utilized for the analysis. We applied a linear combination of L1 and L2 to remove the ionospheric delay. We used 73 GEONET sites in eastern Japan, as shown in Fig. 1. The IGS final precise orbit was adopted for our analysis (Dow et al. 2009).

We conducted two independent analyses with different time periods and sites. In the primary analysis, we estimated spatiotemporal evolution of faults slip in approximately 2 h from 05:00 (UTC) to 06:56 on March 11, using 66 sites denoted by red squares in Fig. 1. To maintain continuity and stability of the analysis, we did not utilize the sites located in a coastal area where data streaming was stopped around 06:25 due to strong shaking and power outage. In addition to the M_w 9.0 mainshock at 05:46, this period includes three large aftershocks in the off Iwate, off-Ibaraki, and the outer rise of the off-Miyagi region. The first M_w 7.4 aftershock (hereafter "Iwate-Oki EQ") occurred off Iwate at 06:08. A few minutes later, the M_w7.8 largest aftershock (hereafter "Ibaraki-Oki")

(See figure on next page.)

Fig. 1 Map of the focal area of the 2011 Tohoku-Oki earthquake. Focal mechanisms represent the mainshock (red), the aftershock in the off-Ibaraki (blue, hereafter "Ibaraki-Oki EQ"), and the aftershock in the off Iwate (green, hereafter "Iwate-Oki EQ") estimated by NIED. Red squares denote the GEONET sites used for the primary analysis. Blue squares are the additional sites used for the analysis of the Iwate-Oki EQ. Gray rectangles show the assumed fault planes. Black and gray dotted lines indicate trench axis and the depth of the plate interface, respectively. Two red arrows in the bottom right corner indicate the direction of the assumed slip basis, which are oriented 25° from plate subduction denoted by the black arrow. Black squares indicate subfaults that are described in the following figure
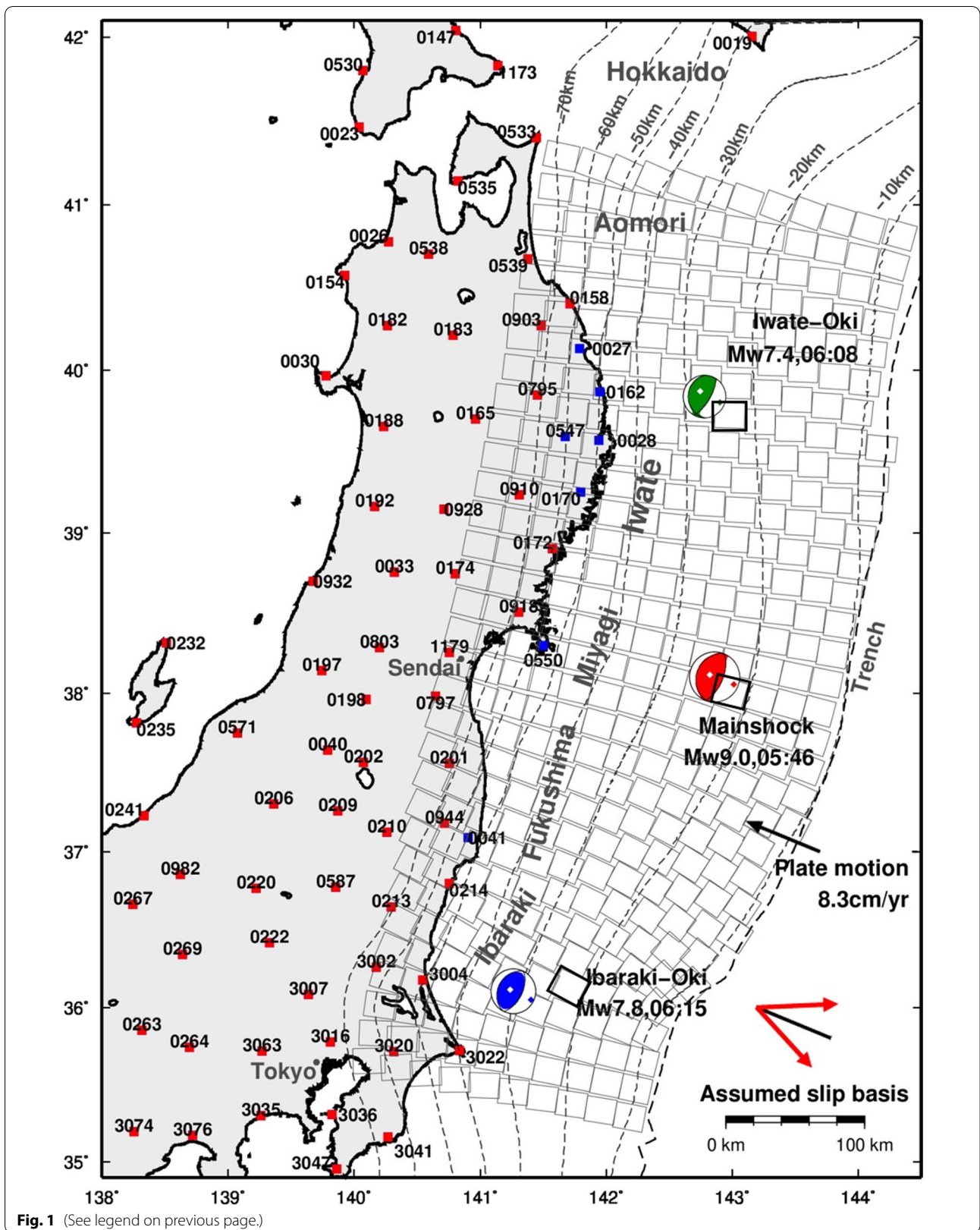
Fig. 1 (See legend on previous page.)

Tanaka *et al. Progress in Earth and Planetary Science* (2022) 9:55

Page 5 of 20

occurred off-Ibaraki at 06:15. Finally, the M_w 7.6 aftershock in the outer rise occurred at 06:25. The CMT solutions proposed by the National Research Institute for Earth Science and Disaster Resilience (NIED) are shown in Fig. 1. They suggested that the mainshock, Iwate-Oki EQ and Ibaraki-Oki EQ demonstrate a thrust slip with a compression axis orienting NNE-SSW. The outer rise aftershock exhibited a normal fault slip with a similar orientation to the compression axis. The primary analysis focuses on the coseismic slip of the mainshock and the Ibaraki-Oki EQ and the early afterslip of the mainshock.

In the case of the Iwate-Oki EQ, seven coastal sites denoted by blue squares in Fig. 1 are essential to maintain a resolution for its minor deformation. Therefore, we conducted an additional analysis using 73 sites, including these coastal sites, from 05:00 to 06:25. Hereafter, we show the results from the additional analysis as the best estimates for the results associated with the Iwate-Oki EQ.

2.2 Observation equation of the PTS

2.2.1 Basic observation equation for a single line of sight

In this section, we describe how the carrier phase observations are connected with unknowns. First, a basic observation equation for a single line of sight was shown, written as Eq. (1). Hereafter, the subscription *s* and superscription *p* represent site and satellite, respectively. Then, now we show the equation for the line between site *s* and satellite *p*. All terms in this equation are in the dimension of length, as it relates the observed variation of carrier phase to change in site-to-satellite range caused by fault slip and other factors such as tropospheric delay. As fault slip is a relative quantity before and after the focused phenomena, Eq. (1) describes the relative variations of all parameters. Please note that this equation does not include error factors such as multipath noise, dispersive delays, oscillator offsets and noise that are not modeled in the current PTS.

$$\lambda \phi_s^p(t) - R_s^p(t) = \mathbf{A}_s^p(t)(\mathbf{G}_s \mathbf{s}(t)) + m_s^p(t) z_s(t) + \lambda N_s^p(t)$$
$$\mathbf{A}_s^p(t) = \left(e_s^p(t), n_s^p(t), u_s^p(t) \right)$$

(1)

The left side represents observations, the relative change in the observed carrier phase for a specific initial epoch. $\phi_s^p(t)$ is the observed GNSS carrier phase value, which is multiplied by its wavelength λ. $R_s^p(t)$ is the reference range. It is the approximate range calculated from the satellite orbit and the assumed initial coordinates of the site. In other words, the reference range represents the expected site-to-satellite range in the case of no site movement since the initial epoch. Further, the subtraction of $R_s^p(t)$ results in a relative change in the carrier phase. We used the daily coordinate of March 10

obtained from static precise point positioning (PPP) analysis for the initial site coordinate. Details of the PPP analysis will be shown in Sect. 2.5.

The right side of the equation represents unknowns, the relative change in the site-to-satellite range caused by fault slip, tropospheric delay, and phase ambiguity. In the first term, $\mathbf{s}(t)$ is the slip on each fault plane. It is converted into displacement in the direction along the surface (e.g., east–west, north–south, and up–down) by Green's function, $\mathbf{G}_s$. Further, the displacement is finally converted into line-of-sight change through geometric translation by matrix $\mathbf{A}_s^p(t)$. It contains a unit vector in the direction of line of sight which is written under the local coordinates along surface at each site. Now, we write the elements of this unit vector as $e_s^p(t)$, $n_s^p(t)$, and $u_s^p(t)$. $z_s(t)$ in the second term is the zenith tropospheric delay, and the coefficient m_s^p is the mapping function. $N_s^p(t)$ in the third term represents the phase ambiguity. Unknown parameters of the PTS are fault slip $\mathbf{s}(t)$, tropospheric delay $z_s(t)$, and phase ambiguity $N_s^p(t)$.

2.2.2 Parameter settings associated with the unknown

For Green's function, $\mathbf{G}$, we used the conventional elastic half-space model proposed by Okada (1992). We assumed 386 rectangular fault patches with an area of approximately 22 km (Fig. 1) along the plate interface model compiled by Kita et al. (2010). In this study, we did not estimate strike-slip and dip-slip on each subfault. In that case, we have to give largely different smoothing strength and process noise values for two components, since the former one will experience much more significant variation in such thrust slip event. Instead, we defined two slip components oriented 25° from the reverse direction of plate subduction, as indicated by the two red arrows in Fig. 1, to apply uniform hyperparameter settings. Additionally, we adopted this acute angle basis to give a smaller degree of freedom for along strike direction, to the estimation stability. We assumed a uniform subduction direction of N67.5°W based on the plate motion vector proposed by MORVEL (DeMets et al. 2010).

Parameter estimation of the PTS is carried out by Kalman filtering. To capture the rapid change in coseismic slip, we assumed a white noise stochastic process for fault slip. We set a process noise value of 3.0 m for both the slip components for the period until the mainshock (before 05:51), and 0.3 m for the period after the mainshock (after 05:51), considering differences of slip magnitude of the mainshock and large aftershocks. A discretized Laplacian spatial smoothing constraint was employed on the slip of each subfault. We also changed the smoothing strength at 05:51. A weaker smoothing was adopted for the period until the mainshock to

catch up with a huge coseismic slip. The process noise values and the smoothing strength were determined through trial and error based on the peak slip, equivalent magnitude, and the root mean squared (RMS) difference between the displacement predicted by the PTS slip and that observed by independent kinematic PPP analysis. Results for the mainshock were utilized to select the period until the mainshock. For the period after the mainshock, results for the Ibaraki-Oki EQ were implemented. Details of the PPP analysis will be shown in Sect. 2.5. Please see also Additional file 2: Text S2, Table S1, Figure S2 to S5, and Equations S2 to S8 for the details of hyperparameter selections.

Niell (1996) model was used for the tropospheric delay mapping function, m. Only the wet component was solved as an unknown parameter. We removed hydrostatic delay as a constant value using the model of Saastamoinen (1972). A random walk with a process noise of 5×10^{-5} m s$^{-1/2}$ was implemented. Finally, white noise was assumed for phase ambiguity, with a process noise of $10^{1/2}$ m.

2.2.3 Expansion toward double differences

Next, explicit observation equations are displayed in the form of vector and matrix, as shown in Eq. (2). As described by this equation, the actual estimation is carried out using simultaneous equations for many lines of sight. Additionally, both sides of the equation are finally transformed into double-differenced values to mitigate common errors, such as the clock. Some previous studies (e.g., Odijk et al. 2016) show that we can mitigate common errors also by using undifferenced observation equations in which various error factors are directly parameterized. However, different from normal positioning, PTS uses the observations between all sites and satellites together to invert them into fault slip. Therefore, to limit number of unknown, PTS carries out a priori elimination of common errors using double difference.

$$\mathbf{d}_k = \mathbf{H}_k * \mathbf{x}_k + \boldsymbol{\beta}_k$$

$$\mathbf{d}_k = \mathbf{D} * \begin{pmatrix} (\lambda\phi - R)_1^1 \\ \vdots \\ (\lambda\phi - R)_{nS}^{np} \end{pmatrix}_k \qquad (2)$$

$$\mathbf{H}_k = (\mathbf{D} * \mathbf{AGD} * \mathbf{mD} * \boldsymbol{\Lambda})_k$$

$$\mathbf{x}_k = \left(s_1 \ldots s_{nB}, z_1 \ldots z_{nS}, N_1^1 \ldots N_{nS}^{nP} \right)_k^T$$

Here, the subscripts k attached to vectors or matrices represent the time. nP, nS, and nB are the total number of satellites, sites, and fault planes used in the estimation, respectively. np is the number of visible satellites at the time $t = k$. Please note that nP and np can be different.

On the left side, the observed carrier phase change for each line of sight was concatenated as the observation vector $\mathbf{d}_k$. $\mathbf{D}$ is the operator matrix used to generate double differences. It extracts values for certain four lines from the observation vector and computes a double difference. In this study, we set one site and satellite as reference and took pairs radially between other sites and satellites. Please note that the operator $\mathbf{D}$ also varies in time as visible satellite changes. On the right side, the design matrix $\mathbf{H}_k$ contains translation matrix $\mathbf{A}$, Green's function $\mathbf{G}$, mapping function matrix $\mathbf{m}$, and extraction operator $\boldsymbol{\Lambda}$. See Additional file 2: Text S1 and Equations S1 for the expressions of these matrices. These coefficients convert each unknown parameter into their azimuthal contribution toward each line of sight, which is identical to the observation vector. Finally, operator $\mathbf{D}$ transforms them into double-differenced values for connection to the observations. The values of elements inside matrices $\mathbf{A}$ and $\mathbf{m}$ vary with time as the direction of the lines varies with the satellite movement. Thus, the design matrix also contains a time subscription. The unknown vector $\mathbf{x}_k$ includes slip on each fault plane, zenith tropospheric delay at each site, and phase ambiguity for each line of sight. $\boldsymbol{\beta}_k$ is the observation noise. As we mentioned before, the Kalman filter estimates the temporal evolution of the above unknowns using the state-space modeling. In addition to forward estimation, we also carried out backward smoothing for the period after the mainshock, to improve stability of early afterslip estimation. See Additional file 2: Text S2, Table S1, and Equations S2 to S8 for the details of application of the state-space modeling.

2.3 Kinematic preservations of coseismic slip

The goal of this study is to continuously estimate co- and postseismic slip. For this objective, another method was considered to preserve the contribution of coseismic slip inside the Kalman filtering during the postseismic period to avoid the trade-off between other unknowns. Hereafter, we refer to this treatment as "reset." First, as shown in Eq. (3), the unknown parameters in the period after the time of reset $t = T_{\text{reset}}$ can be written as two components: values at $t = T_{\text{reset}}$ and variation from them. Now, we omit the indexes of site and satellite in this equation.

$$\lambda\phi(t) - R(t) = \mathbf{A} * (\mathbf{G}(\mathbf{s}(T_{\text{reset}}) + \delta\mathbf{s}(t))) + m(z(T_{\text{reset}}) + \delta z(t)) + \lambda(N(T_{\text{reset}}) + \delta N(t)) \qquad (3)$$

Further, if the Kalman filtering proceeds to $t = T_{\text{reset}}$, we will obtain the estimated unknowns $\mathbf{s}(T_{reset})$, $z(T_{reset})$, and $N(T_{reset})$. Then, in the estimation after $t = T_{\text{reset}}$, we calculate their contribution toward line-of-sight

direction, $R_{reset}(t)$, and subtract it from the observation as shown in Eq. (4). Please note that we calculate $R_{reset}(t)$ at each epoch because **A** and *m* vary in time with satellite movements.

$$\lambda\phi(t) - R(t) - R_{\text{reset}}(t) = \mathbf{A} * (\mathbf{G}\delta\mathbf{s}(t)) + m\delta z(t) + \lambda\delta N(t)$$
$$R_{\text{reset}}(t) = \mathbf{A} * (\mathbf{G}\mathbf{s}(T_{\text{reset}})) + mz(T_{\text{reset}}) + \lambda N(T_{\text{reset}})$$

(4)

In this manner, the proceeding estimation can be transferred to that focusing on the variation after $t = T_{\text{reset}}$. The estimations at $t = T_{\text{reset}}$ will be preserved as the fixed solution, and additional variations $\delta\mathbf{s}(t)$, $\delta z(t)$ and $\delta N(t)$ will result into new unknowns. We carried out "reset" at 05:51, 5 min after the mainshock. We decided this time considering the duration of the mainshock rupture, which has been estimated to be 2–4 min by previous studies using conventional positioning or seismic data (e.g., Hayes (2011), Koketsu et al. (2011), Ammon et al. (2011)).

2.4 Application of sidereal filter to reduce multipath noise

As shown in Eq. (1), the current model of the PTS does not include site movements that are not associated with fault slip. Therefore, apparent movement caused by multipath noise may contaminate the estimated slip time series. In this study, we applied the sidereal filter (e.g., Bock et al. 2000; Choi et al. 2004; Larson et al. 2007) to slip time series obtained by the PTS. We analyzed the carrier phase data of 05:00–07:00 on March 10, under the same parameter settings as the analysis for March 11. Then, following Larson et al. (2007), we removed the high-frequency noise of the obtained slip time series with a 10 s moving average. Finally, we shifted these time series by 236 s, and subtracted them from the slip time series of March 11. Please note that the 10 s moving average is applied only to the time series of March 10. As a result of sidereal filtering, the noise of the slip time series was significantly reduced, especially for a few minutes or longer. See Additional file 2: Text S3 and Figure S6 to S7 for the details of its effect.

2.5 PPP analysis for the initial site coordinates and the reference of displacement

We carried out static and kinematic PPP analysis for each of the 73 GEONET sites used in this study. The GNSS data processing package GIPSY/OASIS (Lichten and Border 1987) version 6.4 was utilized for both two types of analysis. We used the daily coordinates of March 10 obtained by static analysis for the initial site coordinates, which is required to calculate the reference range, translation matrix, and mapping function. We used 1 s kinematic PPP time series to compare displacement by PTS and that by normal positioning. We took differences

between the time series average before and after the event origin. We extracted 05:41–05:46 and 05:51–05:56 for the mainshock, 06:13–06:15 and 06:20–06:22 for the Ibaraki-Oki EQ, and 06:06–06:08 and 06:13–06:15 for the Iwate-Oki EQ, respectively. To compare of the early postseismic displacement, we took differences between 05:51–05:56 and 06:25–06:30.
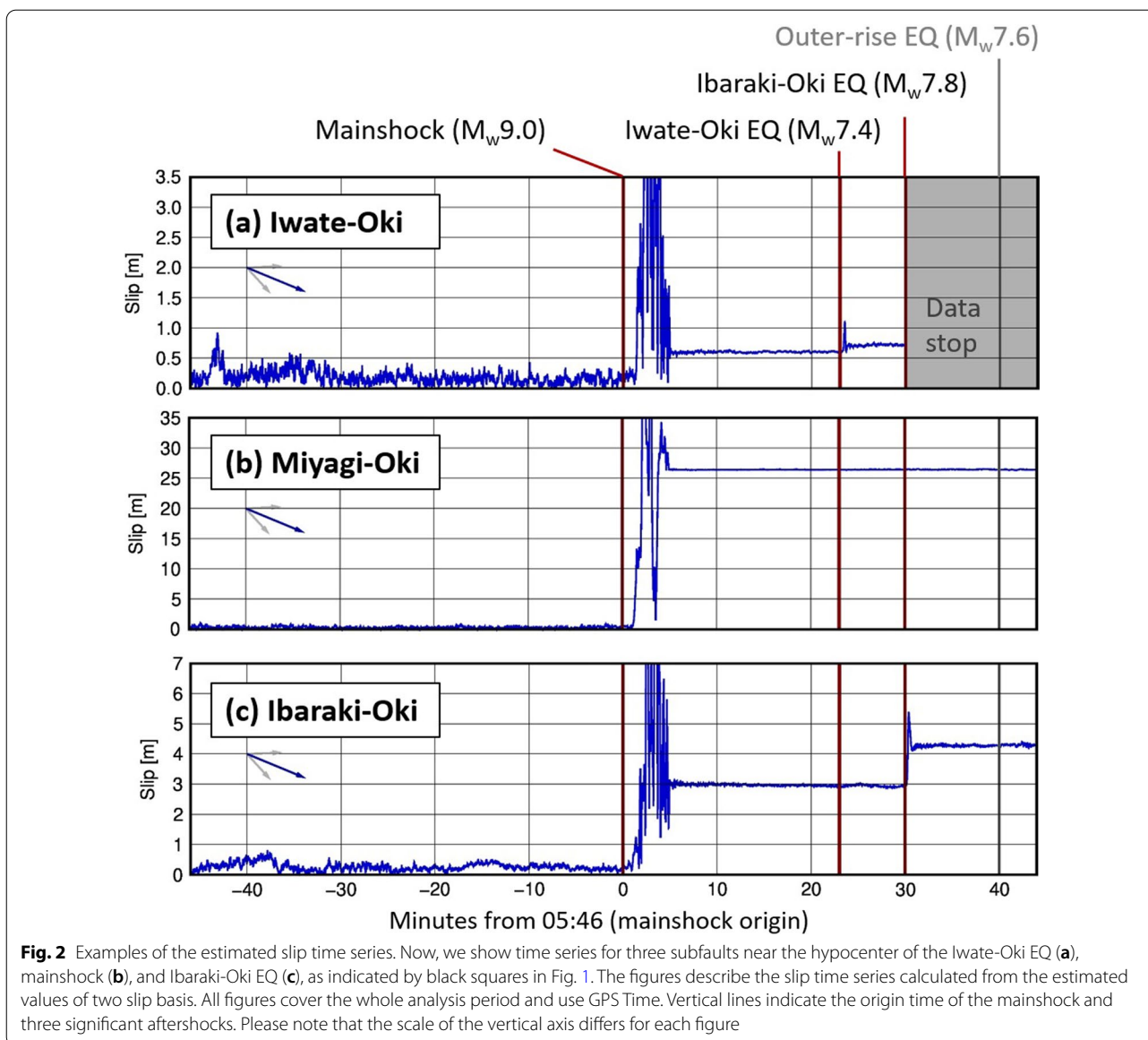
3 Results

3.1 Overview of the estimated slip time series

This section explains the characteristics of the estimated slip time series in detail, implementing a few examples. Firstly, Fig. 2 describes the slip time series for three subfaults near the hypocenter of the mainshock, the Ibaraki-Oki EQ, and the Iwate-Oki EQ. However, it is worth noting that the time series for subfault near the Iwate-Oki is based on results from a slightly different data set which includes an additional seven sites around the coastal area, as mentioned before. Strictly speaking, the following results pertaining to the Iwate-Oki EQ are independent of the others. All of three time series start to increase approximately one min later than the mainshock origin. After that, they overshoot for 3 to 4 min due to seismic waves due to the use of static Green's function. Finally, they show apparent coseismic offsets. Additionally, the time series for Ibaraki-Oki and Iwate-Oki exhibits another offset that corresponds to the origin times of the respective aftershocks. In this way, the PTS successfully detects a series of coseismic slips that occurred in the subduction zone.

Figure 3 demonstrates the slip time series for subfaults in the downdip and northern regions adjacent to the mainshock rupture. Now, we excluded the coseismic offset of the Iwate-Oki EQ and the Ibaraki-Oki EQ to emphasize aseismic small change. See also Figure S8 for raw slip time series including aftershock coseismic slip. As displayed, the downdip region near Iwate and Miyagi shows an apparent postseismic slip increase that reached approximately 0.1–0.2 m. Downdip region near Aomori also exhibits a slip increase, although it is distant from the mainshock rupture. In contrast, subfaults near Ibaraki do not show significant postseismic signals.

As mentioned above, PTS successfully detected both coseismic and early postseismic slips as a continuous time series. As explained in advance, we added a treatment called "reset" to improve the time series stability. It has primarily helped us estimate the coseismic and early postseismic phases precisely. Figure 4 compares the estimated slip time series with and without applying "reset" after the coseismic change. As we can clearly see, slip time series show large drifting amounting to more than few meters in time after the mainshock, in case we do not apply "reset." Updip subfaults (red time series) show

Fig. 2 Examples of the estimated slip time series. Now, we show time series for three subfaults near the hypocenter of the Iwate-Oki EQ (**a**), mainshock (**b**), and Ibaraki-Oki EQ (**c**), as indicated by black squares in Fig. 1. The figures describe the slip time series calculated from the estimated values of two slip basis. All figures cover the whole analysis period and use GPS Time. Vertical lines indicate the origin time of the mainshock and three significant aftershocks. Please note that the scale of the vertical axis differs for each figure

negative drifting, whereas downdip subfaults (blue time series) show positive drifting. Thus, it seems that the coseismic slip which has been once estimated is absorbed by the trade-off between the updip and downdip sides. In contrast, if we apply "reset," the obtained slip time series become more stable and the coseismic slip contribution is preserved correctly. In subsequent chapters, we explain the estimated spatiotemporal evolution of fault slip while comparing it with previous estimations based on conventional positioning.

3.2 Coseismic slip distribution

Figure 5a shows the coseismic slip distribution of the mainshock. Here, the difference between the average slip time series at 05:41–05:46 and 05:51–05:56 was computed. Further, we combined the values of the two components of the slip for each subfault. A peak slip of 26 m was found near the off-Miyagi region. The equivalent moment magnitude was M_w 8.94. The slip vectors mostly pointed toward the ESE, indicating a typical thrust slip. Iinuma et al. (2011) estimated the slip distribution of the mainshock based on daily coordinate time series using conventional GNSS positioning analysis. They showed a peak slip of over 30 m and a magnitude of M_w 9.0. Although some unstable slip direction can be observed in the northern part of the fault zone, our results using PTS are consistent with the results of Iinuma et al. (2011).

Fig. 3 Examples of the estimated early postseismic slip time series. Now, we show time series for the subfaults in the downdip region near Aomori (Line 1), near Iwate (Lines 2 and 3), near Miyagi (Line 4), and near Ibaraki (Line 5), as indicated by black rectangles in the left-side map. All figures display slip time series of 39 min after the mainshock (05:51–06:30 GPS Time) by setting its start as zero. The time series is shown for each subfault along dip direction with a step of 0.5 m. The top side is updip, while the bottom side is downdip. We show slip in the direction of reverse subduction, indicated by blue arrows inside the figures. Brighter color dots represent 5 min moving average of each time series, which is used for drawing Fig. 7. Black and gray vertical lines indicate the origin time of three large aftershocks. Please note that we removed the coseismic slip of the Iwate-Oki EQ and the Ibaraki-Oki EQ, so the time series look continuous without steps
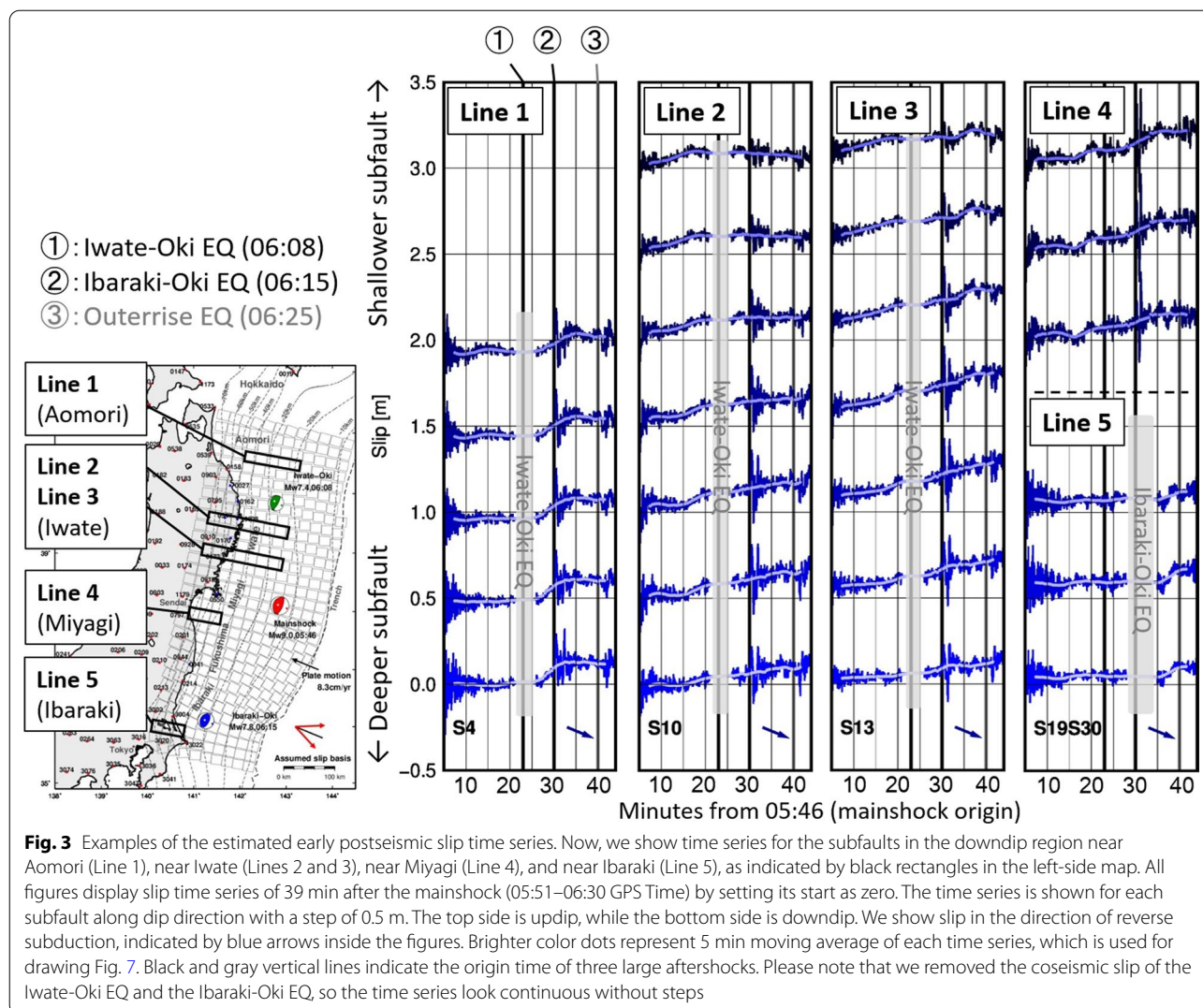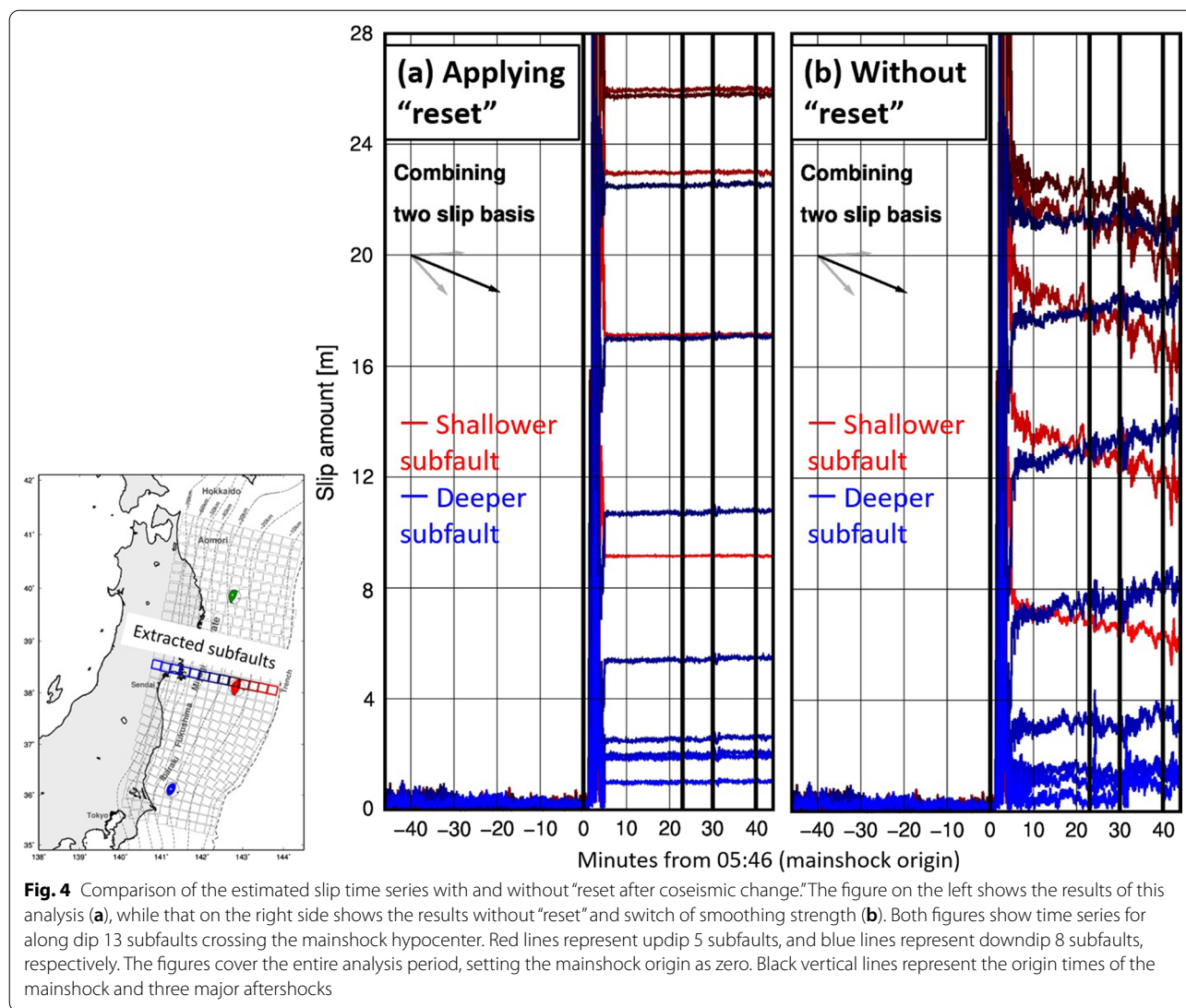
Figure 5 (b) and (c) shows the estimated coseismic slip distributions of the Iwate-Oki and Ibaraki-Oki EQ. Similar to the mainshock, the differences between the slip time series before and after the origin times of each event were described. The difference between the average of 06:06–06:08 and 06:13–06:15, and 06:13–06:15 and 06:20–06:22 was computed for the Iwate-Oki EQ and Ibaraki-Oki EQ, respectively. For the Iwate-Oki EQ, PTS estimated a typical thrust slip of 0.1–0.3 m on an area of approximately 100 km square, highlighted by the black dotted rectangle in Fig. 5 (b). The equivalent seismic moment for this area was of M_w 7.24. For the Ibaraki-Oki EQ, the PTS estimated a thrust slip of 0.2–1.6 m on an area of approximately 150 km square, which is highlighted in the same manner as the Iwate-Oki EQ. The estimated slip area extended toward the updip side of the hypocenter. The equivalent moment magnitude reached M_w 7.72. These moment magnitude values are consistent

with those of Nishimura et al. (2011), M_w 7.24 and 7.76, based on the kinematic PPP time series obtained by conventional positioning analysis. The estimated slip areas also agree well with the single rectangular fault models proposed by Nishimura et al. (2011).

The PTS estimates the time dependence of the slip without estimating the coordinate time series at each GNSS site. The observation is the carrier phase of GNSS itself, and therefore, the agreement between the observed and calculated values is not as straightforward as it would be with conventional positioning. Hence, in Fig. 6, we show comparison between the coseismic displacement expected from the PTS estimation and that obtained from the coordinate time series based on PPP analysis. For each of the three events, the differences between the same time windows as the plot of slip estimated by the PTS are undertaken. In all three events, the displacements showed good agreement between
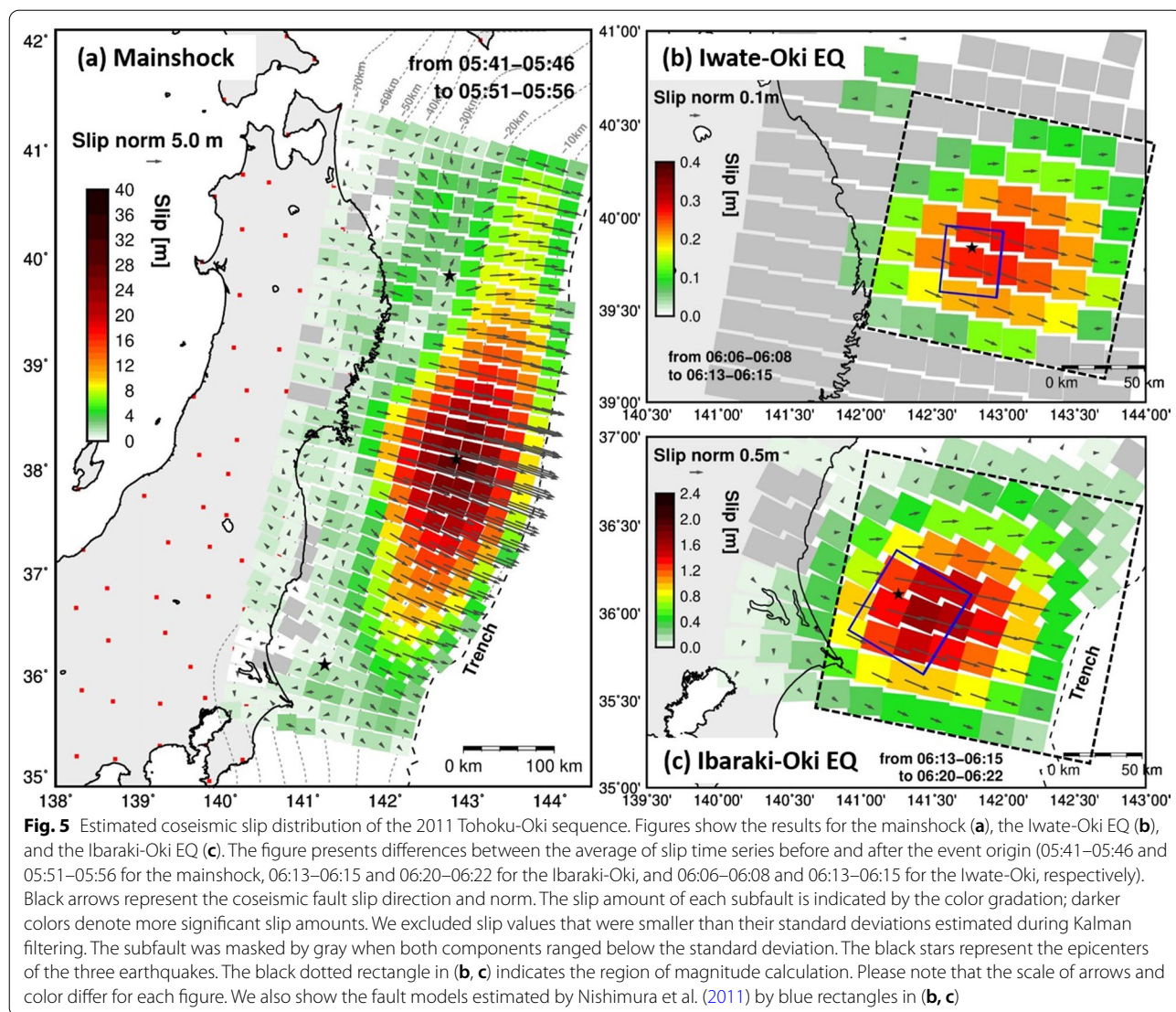
Fig. 4 Comparison of the estimated slip time series with and without "reset after coseismic change." The figure on the left shows the results of this analysis (**a**), while that on the right side shows the results without "reset" and switch of smoothing strength (**b**). Both figures show time series for along dip 13 subfaults crossing the mainshock hypocenter. Red lines represent updip 5 subfaults, and blue lines represent downdip 8 subfaults, respectively. The figures cover the entire analysis period, setting the mainshock origin as zero. Black vertical lines represent the origin times of the mainshock and three major aftershocks

the PTS and PPP. Although the PTS estimated a slightly larger eastward movement and subsidence for the mainshock, the variance reduction (VR) reached 90.8% for all three components. In the case of the Ibaraki-Oki EQ, a VR of 67.5% for 21 sites within 200 km from the epicenter was obtained. In the case of the Iwate-Oki EQ, we obtained a VR of 57.8% for 16 sites within 200 km from the epicenter, despite a much smaller displacement of approximately 7 cm in the maximum.

As shown in the above results, PTS can estimate the coseismic slip distribution of M7 to M9 class earthquakes with an accuracy comparable to that of conventional methods. Moreover, PTS can carry out continuous estimation for more than two earthquakes that occur within just one hour, whereas most previous studies based on normal positioning carried out post

processing for individual event. Our results suggest the capability of PTS for continuous seismic monitoring.

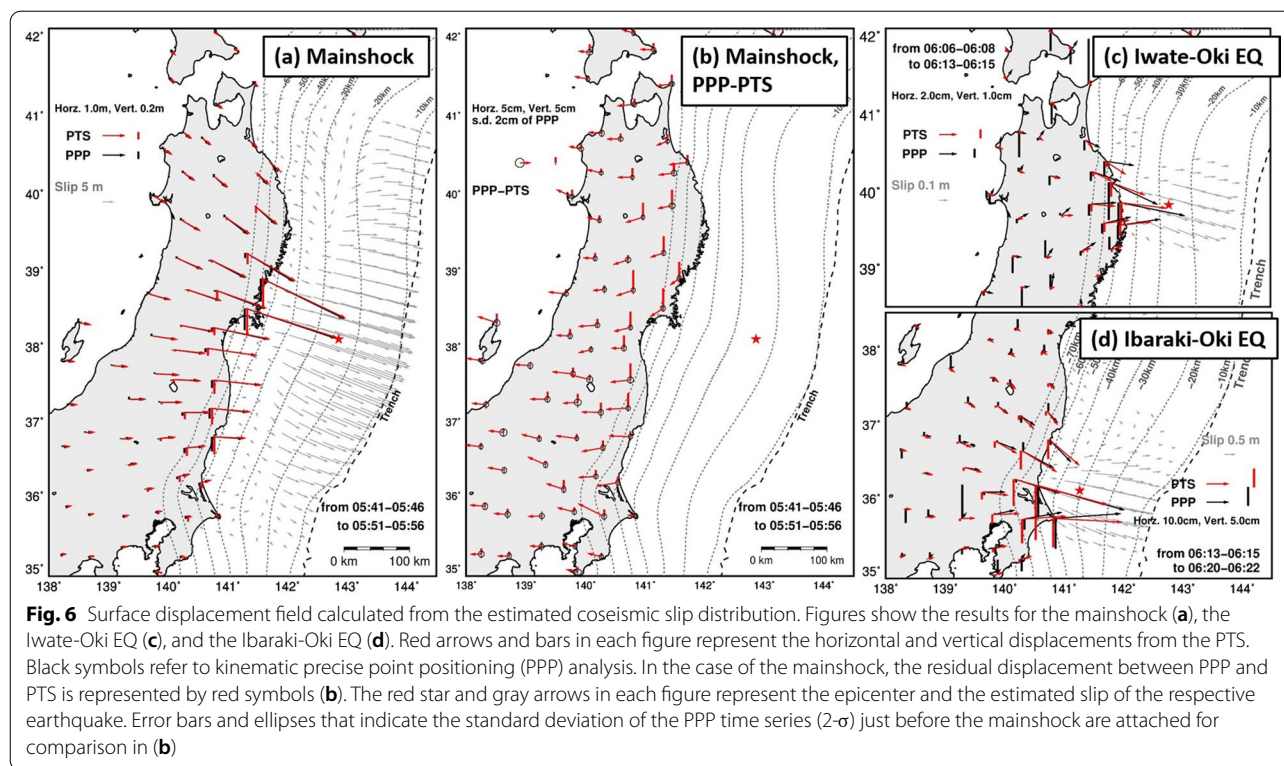### 3.3 Early afterslip distribution following the mainshock

This section describes the details of the early afterslip history estimated by the PTS. Figure 7 shows snapshots of the postseismic slip after the mainshock, excluding aftershock coseismic slip. Here, the moving average of the estimated slip time series using a time window of five min with a step of every 30 s was undertaken. Therefore, the net time length of this result is 34 min. For the northern and southern part of the analyzed region, we excluded slip increase around the time of the Iwate-Oki EQ and the Ibaraki-Oki EQ. Please see Animation S1 for a full animation of the estimated early afterslip. We also show the snapshots including aftershock coseismic

Fig. 5 Estimated coseismic slip distribution of the 2011 Tohoku-Oki sequence. Figures show the results for the mainshock (**a**), the Iwate-Oki EQ (**b**), and the Ibaraki-Oki EQ (**c**). The figure presents differences between the average of slip time series before and after the event origin (05:41–05:46 and 05:51–05:56 for the mainshock, 06:13–06:15 and 06:20–06:22 for the Ibaraki-Oki, and 06:06–06:08 and 06:13–06:15 for the Iwate-Oki, respectively). Black arrows represent the coseismic fault slip direction and norm. The slip amount of each subfault is indicated by the color gradation; darker colors denote more significant slip amounts. We excluded slip values that were smaller than their standard deviations estimated during Kalman filtering. The subfault was masked by gray when both components ranged below the standard deviation. The black stars represent the epicenters of the three earthquakes. The black dotted rectangle in (**b**, **c**) indicates the region of magnitude calculation. Please note that the scale of arrows and color differ for each figure. We also show the fault models estimated by Nishimura et al. (2011) by blue rectangles in (**b, c**)

slip in Figure S9. A blowup of the final slip distribution in 34 min and seismic moment time series of significant slip areas is shown in Figure S10. Slip increase initially appeared in the region near Iwate at approximately 06:00, which exceeds the noise level at approximately 06:10 (2nd to 4th snapshots in the figure, hereafter slip area "B"). It shows a roughly constant increase reaching a final slip of 0.21 m and a M_w of 7.27 in this region. The down-dip region near Miyagi shows a later slip increase starting at approximately 06:10, then exceeds the noise level at approximately 06:15 (4th to 5th snapshots, hereafter slip area "C"). Unlike the slip area B, this area slightly slows down in the final stage of the analysis period. It finally reaches 0.18 m at peak slip and M_w 7.17. Another slip area can be observed near Aomori (5th to 6th snapshots, hereafter slip area "A"). It appears at approximately 06:15

and reaches 0.17 m at peak slip and M_w 7.17, released mainly around 30 min after the mainshock. However, this region may have a lower resolution since it is far from the onshore GNSS sites than other slip areas. Additionally, the subfaults near Ibaraki (hereafter slip area "D") also show thrust slip. However, its amount is small, and only three subfaults exceed the estimated uncertainty. We can also observe a slip in the region near Fukushima in the earlier stage of the analysis period. However, slip time series in this area are unstable and decrease later. Hereafter we mainly discuss other slip areas A, B, and C.

As mentioned above, the PTS estimated early afterslip for several regions adjacent to the mainshock rupture. Additionally, the PTS estimated different onset times of the early afterslip for each slip area. This is an innovative characteristic that has not been suggested in previous studies.

Fig. 6 Surface displacement field calculated from the estimated coseismic slip distribution. Figures show the results for the mainshock (**a**), the Iwate-Oki EQ (**c**), and the Ibaraki-Oki EQ (**d**). Red arrows and bars in each figure represent the horizontal and vertical displacements from the PTS. Black symbols refer to kinematic precise point positioning (PPP) analysis. In the case of the mainshock, the residual displacement between PPP and PTS is represented by red symbols (**b**). The red star and gray arrows in each figure represent the epicenter and the estimated slip of the respective earthquake. Error bars and ellipses that indicate the standard deviation of the PPP time series (2-σ) just before the mainshock are attached for comparison in (**b**)

Next, we compare the estimation by PTS and conventional positioning. Although few studies have analyzed the early postseismic phase, there exist two studies conducted previously on the 2011 Tohoku-Oki earthquake. Munekane (2012) estimated the early afterslip distribution from a conventional positioning time series, which was analyzed by principal component analysis. He found the afterslip immediately after the earthquake, which occurred in the first 10 min between the mainshock and the Iwate-Oki earthquake. An initial afterslip was suggested which extended toward the downdip and north of the mainshock rupture. Further, a peak slip of 4.7 cm and M_w7.08 in 10 min was estimated by the above-mentioned study. Mitsui and Heki (2013) also investigated the early postseismic displacement of 26 min after the mainshock using kinematic PPP time series for GNSS sites in the coastal regions of Iwate and Miyagi. The estimated slip was 0.1 to 0.2 m and equivalent to M_w 7.2–7.3, assuming two fault planes below the analyzed region.

If we compare these results, the slip areas B and C estimated by PTS overlap well with the slip distribution suggested by Munekane (2012). Although the focused analysis region essentially differs, the slip area B also intersects with the fault model suggested by Mitsui and Heki (2013). Although it is below the estimated standard deviation, PTS estimated an approximately 8–10 cm slip increase in the same time window as Munekane (2012)

(see the first and the third snapshot in Fig. 7). This value is approximately twice the value estimated by Munekane (2012). On the other hand, the final moment magnitude appears to be similar considering its time length. Here, a 3.4 times more extended analysis period than Munekane (2012) is observed, with a PTS estimated at M_w 7.42, for the slip area B and C. This moment value is 3.3 times larger than Munekane (2012). Additionally, slip of 0.1 to 0.2 m in 26 min suggested by Mitsui and Heki (2013) is very similar to our results, 0.1 to 0.2 m in 34 min. As stated above, PTS estimated early afterslip in a location similar to that in previous studies based on conventional positioning (Munekane 2012; Mitsui and Heki 2013) and suggested a slightly larger or similar slip magnitude.

Finally, a comparison of the early postseismic displacement from the PTS and that obtained from the kinematic PPP time series is demonstrated in Fig. 8. In the case of PTS, the displacement fields expected from each of the four slip areas are also exhibited. For PPP, the displacement during the Iwate-Oki and the Ibaraki-Oki EQ was excluded. Figure 8 indicates that the early afterslip estimated by PTS provides coherent eastward movement and subsidence for several sites. The maximum horizontal displacement was approximately 4 cm. Slip area B and C provided most of the expected displacement. The slip area A shows a smaller contribution only toward the displacement around Aomori and northern Iwate. In
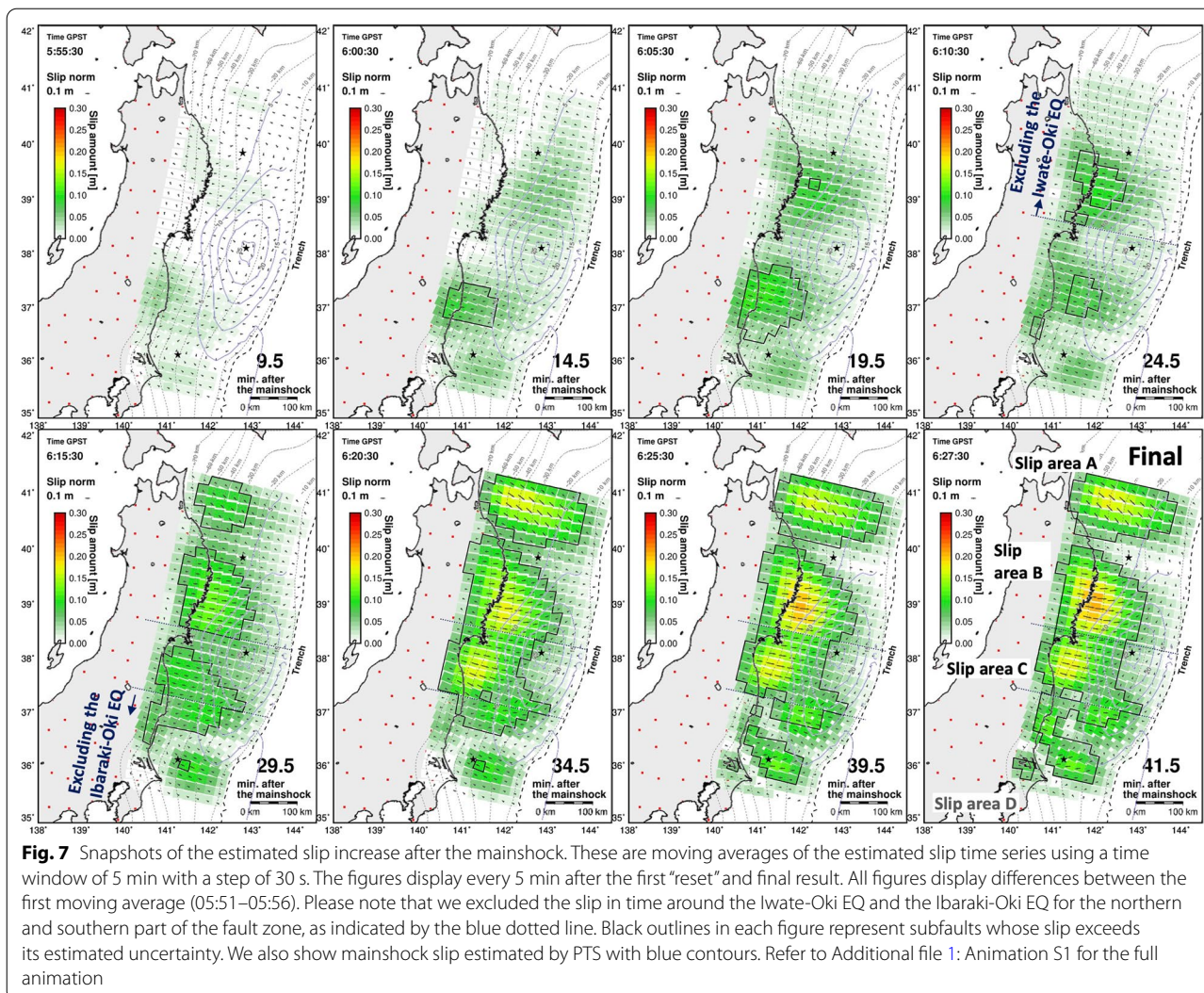
Fig. 7 Snapshots of the estimated slip increase after the mainshock. These are moving averages of the estimated slip time series using a time window of 5 min with a step of 30 s. The figures display every 5 min after the first "reset" and final result. All figures display differences between the first moving average (05:51–05:56). Please note that we excluded the slip in time around the Iwate-Oki EQ and the Ibaraki-Oki EQ for the northern and southern part of the fault zone, as indicated by the blue dotted line. Black outlines in each figure represent subfaults whose slip exceeds its estimated uncertainty. We also show mainshock slip estimated by PTS with blue contours. Refer to Additional file 1: Animation S1 for the full animation

the PPP time series case, the obtained displacement field appears to be much noisier than the PTS. Although few sites show eastward movement, their directions seem to be unstable. The vertical component is noisier than the horizontal component in PPP results. However, the overall character of the horizontal displacement is partially consistent with both within the error ellipsoid of the kinematic PPP time series.

As explained, we estimated the coseismic and early postseismic slip phenomena of the 2011 Tohoku-Oki sequence continuously with high temporal resolution. There is no previous case of such broadband estimation ranging from a timescale of a few minutes to a few tens of minutes. Particularly, the most important contribution of our results is that we obtained spatiotemporal evolution of early afterslip within one hour, which has almost never been unraveled by previous studies. As mentioned before, our results suggest spatial heterogeneity of the onset time of afterslip. This is an innovative characteristic of our results. Moreover, in terms of slip area and total slip amount at certain times, most of our results exhibit comparable precision to post-processed estimation based on the conventional positioning analysis suggested by previous studies. It ensures the reliability of our results.

(See figure on next page.)
Fig. 8 Surface displacement field calculated from the estimated early afterslip. Each figure shows displacement that is expected by slip area A (**a**), B (**b**), C (**c**), and the sum of them (**d**), respectively. Gray arrows indicate the corresponding afterslip in each area. For comparison, PPP displacement is shown in (d). It was calculated from the same time window as PTS analysis but excluding displacement of the Iwate-Oki EQ and the Ibaraki-Oki EQ. Error bars and ellipses that indicate the standard deviation of the PPP time series (2-σ) just before the mainshock are attached
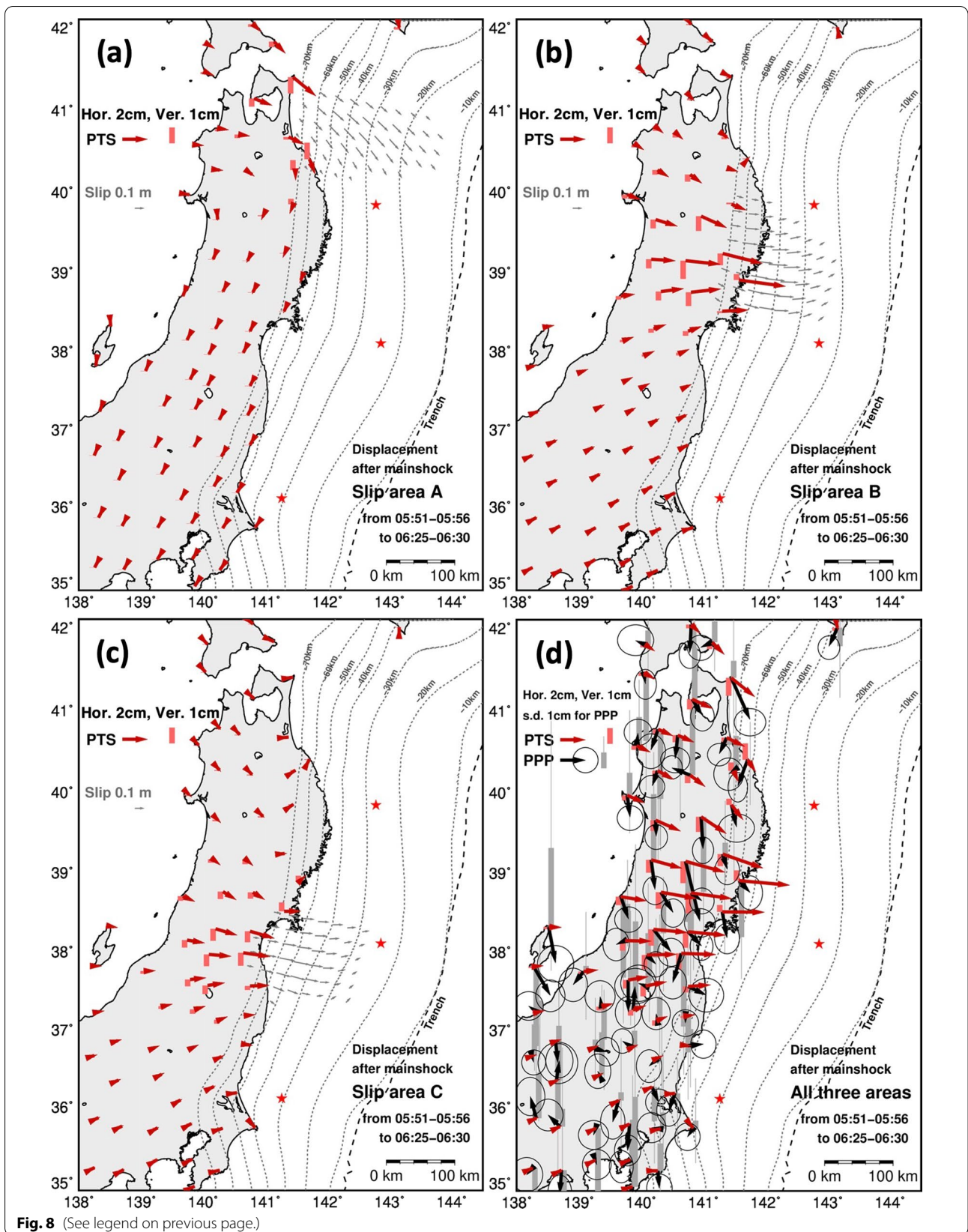
Fig. 8 (See legend on previous page.)

In the next chapter, we discuss future prospective for slip monitoring based on the PTS.

4 Discussion

4.1 Estimation of coseismic slip

In this study, we successfully estimated a series of coseismic slips in the subduction zone using the PTS method. The estimated slip, magnitude, and displacement are consistent with conventional positioning. Our results indicate the capability of the PTS method for continuous seismic monitoring. If we measure the detection limit of the fault slip, we can use two types of standard deviations. One is from the estimation inside the Kalman filter, and the other is the calculation from the obtained slip time series. In this analysis, the former is around 0.1 to 1.6 m, and the latter is 0.1 to 0.4 m for the time before the mainshock. They are equivalent to M_w 6.2–7.0 per subfault. This seems to be a similar threshold to the estimation based on conventional positioning. For future practical use of the PTS, the requirement to add a method to automatically detect coseismic slip offsets may be mandatory. It will also be related to the decision of the time of "reset after the coseismic change." Therefore, it is essential to evaluate the estimation uncertainty of the PTS and discuss regarding setting the threshold for coseismic slip detection. Additionally, since we used static Green's function in our estimations, the slip time series clearly show large overshoot in the few minutes just after the earthquake origin. To avoid contamination of early afterslip time series, handling of dynamic motion associated with coseismic phase is important future work.

4.2 Estimation of early postseismic slip

The PTS also estimated the postseismic slip increase in time after the mainshock. As shown in the previous section, several slip areas appeared adjacent to the mainshock rupture. These slip areas overlap with the early afterslip areas deduced from the conventional positioning in Munekane (2012) and Mitsui and Heki (2013). Compared to Munekane (2012), the result obtained by the PTS shows a slightly larger slip magnitude. Another difference is the splitting of slip area B and C as suggested by PTS. However, initially we set weak spatial smoothing and white noise stochastic processes to correctly estimate the coseismic slip of two large aftershocks. Therefore, it is not surprising that we obtained a larger slip magnitude and rougher slip distribution. If we apply stronger smoothing, ignoring the coseismic slip of the two aftershocks, the obtained slip distribution is observed to be similar to that of Munekane (2012). Further optimization of hyperparameters can be considered, such as introducing the time-dependent stochastic process as suggested by Fukuda et al. (2004).

Unlike the 10-min slip distribution suggested by Munekane (2012), PTS also suggested some postseismic slip around the region near Aomori (slip area A). Their existence can be reasonable because our analysis demonstrated a more extended period. Additionally, Munekane (2012) also estimated the early afterslip distribution in 4 h from 06:30, just after the end of our analysis. Further, in that case, he suggested postseismic slip also in the region offshore Iwate and Aomori, which are similar to our results by PTS. Thus, there is a possibility that we detected the onset of this slip area that were not directly captured by two estimations in Munekane (2012).

However, in the region near Aomori, the reliability of the estimation must be properly evaluated. In this area, the estimated slip direction does not show a clear thrust slip sense, but points toward the southeast. Additionally, its expected contribution toward displacement is minimal despite the considerable slip magnitude, as shown in Fig. 8. This area is the furthest location from onshore GNSS sites, where the strike angle of the plate interface vastly changes. Thus, we should carefully search for the resolution of this area and errors in Green's function. To discuss the slip in this area, we probably need to improve Green's function, including the 3-D structure, as suggested by Hori et al. (2021).

To carry out discussion connected with previous studies, which searched for the later phase of postseismic slip phenomena, the analysis period should be extended. One of the advantages of PTS is its temporal resolution. It provides successive estimations based on Kalman filtering, whereas most previous studies carried out postprocessed inversion for the total slip in a certain period. Further improvement of the estimation precision will help us discuss each slip area's exact onset time, the transition process from coseismic to postseismic processes, and its controlling friction properties. Another important topic is the interaction between afterslip and aftershocks. Although we have shown the coseismic slip of two major aftershocks (the Iwate-Oki EQ and the Ibaraki-Oki EQ) and the early afterslip separately in the previous sections, they are both postseismic process of the M9 mainshock and potentially related. We should make further comparison between the aftershock activity and the early afterslip evolution to clarify their physical relationship.

4.3 Prospects of the PTS method

As stated in the introduction, the PTS method estimates the fault slip and various other parameters in parallel. This means that we can evaluate the contributions of all unknown parameters together. For example, we presently describe the average contribution amount of each parameter among the calculated carrier phases in Fig. 9 (see Additional file 2: Text S5 and Equations

S9 to S12 for the method of their calculation). Fault slip contributes approximately 0.6 m on an average, equivalent to 25%–30% of the total calculated carrier phase in time after the mainshock. If we calculate the contribution of the fault slip on each subfault separately, we can obtain a resolution map of this estimation. Phase ambiguity occupies the largest contribution of more than 1.1 m and approximately 60–90% throughout the analysis period. Thus, we can expect that the refined ambiguity resolution can significantly improve PTS precision. Finally, the tropospheric delay was only 4 cm and 5–10%. It is the smallest but still in the same order of magnitude as the expected displacement given by the early afterslip (see Fig. 8). Upgrading the tropospheric delay mapping function can further refine our estimation of aseismic small slip phenomena.

PTS can also quantify the uncertainty and correlation of unknown parameters through a covariance matrix, estimated together with the state vector. This is beneficial for the search for the trade-off between each unknown parameter. We show an example of the covariance matrix in Fig. 10, normalized to the correlation coefficient matrix. We now adopt the Pearson product-moment correlation coefficient. It describes the values at 05:40 using color scale. As shown in the figure, the phase ambiguity of each site-to-satellite path generally shows a negative correlation. This is because each path is related to another path by a double difference. We can search for error propagation via double difference and consider the optimum baseline setting to mitigate its influence. Tropospheric delay at each site showed a strong positive correlation, implying that they were nearly uniform. We can also observe some amount of correlation between tropospheric delay and fault slip, indicating that a trade-off between them may occur. We must search for the situation and impact of the trade-off to consider its mitigation.
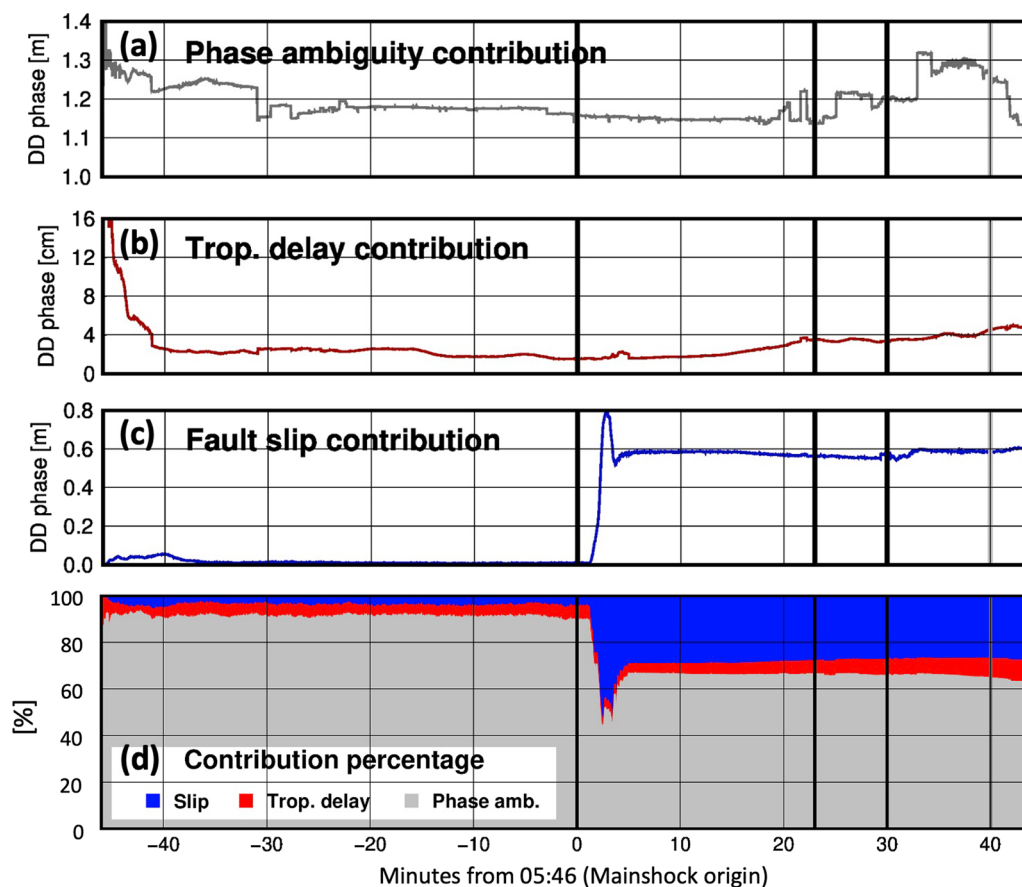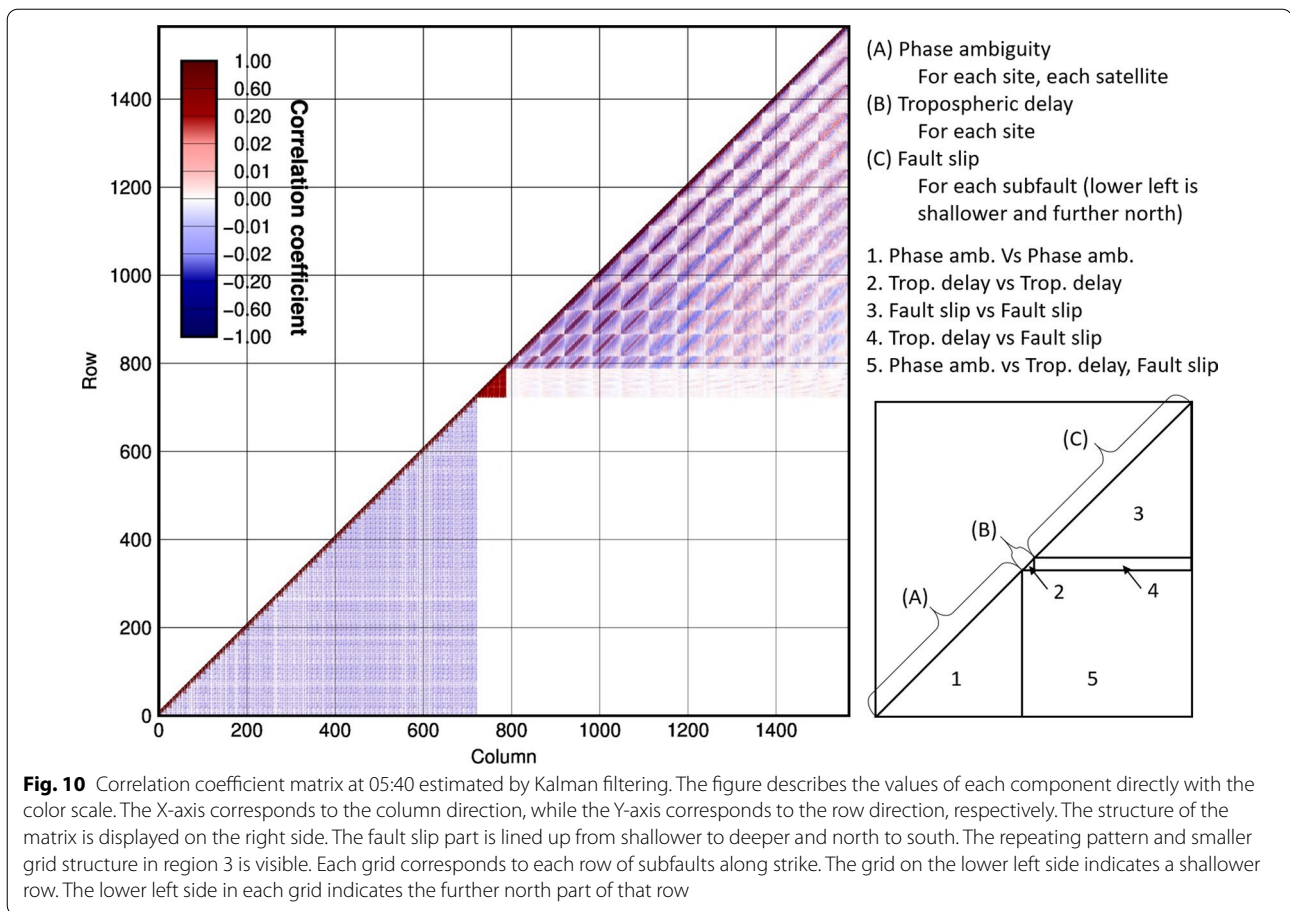

Fig. 9 Time evolution of the expected contribution of each unknown among the calculated carrier phase. The figures describe the average absolute value of contribution for all double difference. Four figures represent the contribution of phase ambiguity (**a**), tropospheric delay (**b**), fault slip (**c**), and their percentage among total calculated carrier phase (**d**). The vertical width of the three colored regions in (**d**) represents the percentage of each unknown. Please note that the contribution of ionospheric delay is not present here because we removed it using dual-frequency combination. Refer to Additional file 2 for the calculation of these contribution values

Fig. 10 Correlation coefficient matrix at 05:40 estimated by Kalman filtering. The figure describes the values of each component directly with the color scale. The X-axis corresponds to the column direction, while the Y-axis corresponds to the row direction, respectively. The structure of the matrix is displayed on the right side. The fault slip part is lined up from shallower to deeper and north to south. The repeating pattern and smaller grid structure in region 3 is visible. Each grid corresponds to each row of subfaults along strike. The grid on the lower left side indicates a shallower row. The lower left side in each grid indicates the further north part of that row

Finally, the fault slip shows a strong correlation between the neighboring subfaults. However, the correlation pattern oscillates from negative to positive and sometimes indicates a correlation between distant subfaults. It is possible that such a complicated correlation is controlled mainly by spatial smoothing constraints. Although PTS itself is not a problem, we should carefully check such trade-offs between subfaults to discuss the resolution of the estimation.

As shown above, we can obtain various insights into parameter separation in PTS. This comprehensive description is complex in the case of conventional positioning. Detailed evaluation and discussion of parameter separation remain an interesting future work to improve the accuracy of the PTS method. Additional important topic is an extension of the model inside PTS to include error factors such as hardware delays, receiver phase bias, and satellite phase bias that are ignored in current observation equation. As pointed out by Odijk et al. (2016), use of double difference makes error propagation complicated and prevents intuitive understanding of results. Use of undifferenced observation equation is additional future topic. Quantitative evaluation of parameter separation will be also helpful for carrying out such future works.

5 Conclusions

We investigated broadband fault slip monitoring based on the PTS method to invert fault slip directly from variations in the GNSS carrier phase. In this study, we applied the PTS method to the coseismic and early postseismic slip phenomena of the 2011 Tohoku-Oki sequence. We estimated the spatiotemporal evolution of fault slip for approximately 2 h before and after the mainshock origin, using 1 Hz carrier phase data of 73 GNSS sites in east Japan. As a result, the PTS successfully estimated the series of coseismic slip of the M_w 9.0 mainshock, M_w 7.8 largest aftershock in the off-Ibaraki region, and M_w 7.4 third-largest aftershock in the off Iwate region. For all three events, the estimated slip distribution, equivalent moment magnitude, and calculated displacement field showed comparable accuracy with respect to the conventional positioning. These results suggest the capability of PTS for continuous seismic monitoring.

Tanaka *et al. Progress in Earth and Planetary Science*   (2022) 9:55

Page 18 of 20

Additionally, the PTS also estimated the postseismic slip increase in time just after the mainshock. The slip increase mainly appears in the region adjacent to the mainshock rupture. We obtained three major slip areas around the downdip region near Aomori, Iwate, and Miyagi. The slip amount is approximately a maximum of 0.2 m and equivalent to M_w 7.4 in 34 min after the mainshock, for the slip areas near Iwate and Miyagi. These cumulative slip amounts seem to be similar or slightly larger than the estimations based on conventional positioning. The locations of the obtained slip areas also well overlap. In this manner, we succeeded in the continuous estimation of coseismic and early postseismic slip phenomena with a timescale of a few minutes to an hour and an amplitude of less than 1 m to over 10 or 20 m. Particularly, we obtained spatiotemporal evolution of early afterslip within one hour, which has almost never been unraveled by previous studies. Our results indicate the excellent capability of the PTS method for broadband fault slip monitoring and its potential contribution to investigating early postseismic phenomena. Although this study mainly focused on estimating the fault slip, the major advantage of this method is the quantitative evaluation of the separation and contribution of all unknown parameters. Based on this advantage, further improvements must be made to refine the results and extend the application of PTS.

Abbreviations
GEONET: GNSS Earth Observation Network; GNSS: Global Navigation Satellite System; GPS: Global Positioning System; IGS: International GNSS Service; MORVEL: Mid-Ocean Ridge VELocity; NIED: National Research Institute for Earth Science and Disaster Resilience; PPP: Precise Point Positioning; PTS: Phase To Slip; VADASE: Variometric Approach for Displacements Analysis Stand-alone Engine.

Supplementary Information
The online version contains supplementary material available at https://doi.org/10.1186/s40645-022-00514-2.

Additional file 1. In this file, we describe the details of the formulation of PTS and selection of hyperparameters used in the analysis. We also show the effect of sidereal filter and some additional figures associated with the early afterslip estimated by PTS.

Additional file 2. It show a full animation describing the spatio-temporal evolution of the early afterslip estimated by PTS. It uses the same expression as the snapshots in the main text, but showing temporal evolution in every 30 s.

Author contributions
YT carried out the main part of the analysis. YO and SM helped the interpretation of the results and the planning for the research. YT and YO drafted the manuscript. All authors read and approved the final manuscript.

Availability of data and materials
We are grateful to the Geospatial Information Authority of Japan (GSI) and Japan Association of Surveyors for providing GNSS Earth Observation Network (GEONET) data. It can be found at https://www.jsurvey.jp/eng-data_rinex-1sec.htm or https://www.gpsdata.co.jp. The former one has a website in English, whereas the latter one is only in Japanese. Please note that the 1-Hz carrier phase data of the GEONET are not open but charged. It is the product to be purchased through several private companies or associations, mainly for the public survey. We are also very grateful to the International GNSS Service (IGS) for providing high-quality precise orbit information. It can be found at https://cddis.nasa.gov/Data_and_Derived_Products/GNSS/orbit_products.html.

Declarations

Competing interests
The authors declare that they have no competing interest.

Author details
[1]Solid Earth Physics Laboratory, Graduate School of Science, Tohoku University, 6-3 Aza-Aoba, Aramaki, Aoba-ku, Sendai 980-8578, Japan. [2]Research Center for Prediction of Earthquakes and Volcanic Eruptions, Graduate School of Science, Tohoku University, 6-6 Aza-Aoba, Aramaki, Aoba-ku, Sendai 980-8578, Japan. [3]Division for the Establishment of Frontier Sciences of Organization for Advanced Studies, Tohoku University, 2-1-1 Katahira, Aoba-ku, Sendai 980-8577, Japan. [4]International Research Institute of Disaster Science, Tohoku University, Aoba 468-1, Aramaki, Aoba-ku, Sendai 980-8572, Japan. [5]Division of Earth and Planetary Sciences, Department of Geophysics, Graduate School of Science, Kyoto University, Kitashirakawa-Oiwake-cho, Sakyo-ku, Kyoto 606-8502, Japan.

References
Allen RM, Ziv A (2011) Application of real-time GPS to earthquake early warning. Geophys Res Lett 38(16):L16310. https://doi.org/10.1029/2011GL047947

Ammon CJ, Lay T, Kanamori H, Cleveland M (2011) A rupture model of the 2011 off the Pacific coast of Tohoku Earthquake. Earth Planet Space 63(7):693–696. https://doi.org/10.5047/eps.2011.05.015

Barnhart WD, Murray JR, Briggs RW, Gomez F, Miles CPJ, Svarc J, Riquelme S, Stressler BJ (2016) Coseismic slip and early afterslip of the 2015 Illapel, Chile, earthquake: implications for frictional heterogeneity and coastal uplift. J Geophys Res 121(8):6172–6191. https://doi.org/10.1002/2016JB013124

Blewitt G, Kreemer C, Hammond WC, Plag HP, Stein S, Okal E (2006) Rapid determination of earthquake magnitude using GPS for tsunami warning systems. Geophys Res Lett 33:L11309. https://doi.org/10.1029/2006GL026145

Blewitt G, Hammond WC, Kreemer C, Plag HP, Stein S, Okal E (2009) GPS for real-time earthquake source determination and tsunami warning systems. J Geod 83(3–4):335–343. https://doi.org/10.1007/s00190-008-0262-5

Bock Y, Nikolaidis RM, de Jonge PJ, Bevis M (2000) Instantaneous geodetic positioning at medium distances with the Global Positioning System.

Tanaka *et al. Progress in Earth and Planetary Science*   (2022) 9:55

Page 19 of 20

J Geophys Res Solid Earth 105(B12):28223–28253. https://doi.org/10.1029/2000JB900268

Bock Y, Prawirodirdjo L, Melbourne TI (2004) Detection of arbitrarily large dynamic ground motions with a dense high-rate GPS network. Geophys Res Lett 31(6):L06604. https://doi.org/10.1029/2003GL019150

Bürgmann R, Segall P, Lisowski M, Svarc J (1997) Postseismic strain following the 1989 Loma Prieta earthquake from GPS and leveling measurements. J Geophys Res 102(B3):4933–4955. https://doi.org/10.1029/96JB03171

Bürgmann R, Ergintav S, Segall P, Hearn EH, McClusky S, Reilinger RE, Woith H, Zschau J (2002) Time-dependent distributed afterslip on and deep below the Izmit earthquake rupture. Bull Seism Soc Am 92(1):126–137. https://doi.org/10.1785/0120000833

Cervelli P, Segall P, Johnson K, Lisowski M, Miklius A (2002) Sudden aseismic fault slip on the south flank of Kilauea volcano. Nature 415(6875):1014–1018. https://doi.org/10.1038/4151014a

Choi K, Bilich A, Larson KM, Axelrad P (2004) Modified sidereal filtering: implications for high-rate GPS positioning. Geophys Res Lett 31(22):L22608. https://doi.org/10.1029/2004GL021621

Colosimo G, Crespi M, Mazzoni A (2011) Real-time GPS seismology with a stand-alone receiver: a preliminary feasibility demonstration. J Geophys Res 116(B11):B11302. https://doi.org/10.1029/2010JB007941

DeMets C, Gordon RG, Argus DF (2010) Geologically current plate motions. Geophys J Int 181(1):1–80. https://doi.org/10.1111/j.1365-246X.2009.04491.x

Dow JM, Neilan RE, Rizos C (2009) The international GNSS service in a changing landscape of global navigation satellite systems. J Geod 83(3–4):191–198. https://doi.org/10.1007/s00190-008-0300-3

Freed AM, Bürgmann R, Calais E, Freymueller J, Hreinsdóttir S (2006) Implications of deformation following the 2002 Denali, Alaska, earthquake for postseismic relaxation processes and lithospheric rheology. J Geophys Res Solid Earth 111(B1):B01401. https://doi.org/10.1029/2005JB003894

Fukuda J, Higuchi T, Miyazaki S, Kato T (2004) A new approach to time-dependent inversion of geodetic data using a Monte Carlo mixture Kalman filter. Geophys J Int 159(1):17–39. https://doi.org/10.1111/j.1365-246X.2004.02383.x

Hatanaka Y, Tsuji H, Iimura Y, Kobayashi K, Morishita H (1996) Application of GPS kinematic method for detection of crustal movements with high temporal resolution. In: GPS trends in precise terrestrial, airborne, and spaceborne applications, international association of geodesy symposia, symposium no. 115, 3–4 July, 1995, Boulder, Colorado, USA, pp 105–109. https://doi.org/10.1007/978-3-642-80133-4_17

Hayes GP (2011) Rapid source characterization of the 2011 M_w 9.0 off the Pacific coast of Tohoku Earthquake. Earth Planet Space 63:529–534. https://doi.org/10.5047/eps.2011.05.012

Helmstetter A, Shaw BE (2009) Afterslip and aftershocks in the rate-and-state friction law. J Geophys Res Solid Earth 114(B1):B01308. https://doi.org/10.1029/2007JB005077

Hirahara K, Nakano T, Hoso Y, Matsuo S, Obana K (1994) An experiment for GPS strain seismometer. In: Japanese symposium on GPS, 15–16 December, Tokyo, Japan, pp 67–75

Hirata Y, Ohta Y (2016) Spatial and temporal characteristics of optimum process noise values of tropospheric parameters for kinematic analysis of Global Navigation Satellite System (GNSS) sites in Japan. Earth Planet Space 68(1):203. https://doi.org/10.1186/s40623-016-0578-y

Hirose H, Hirahara K, Kimata F, Fujii N, Miyazaki S (1999) A slow thrust slip event following the two 1996 Hyuganada earthquakes beneath the Bungo Channel, southwest Japan. Geophys Res Lett 26(21):3237–3240. https://doi.org/10.1029/1999GL010999

Hori T, Agata R, Ichimura T, Fujita K, Yamaguchi T, Iinuma T (2021) High-fidelty elastic Green's functions for subduction zone models consistent with the global standard geodetic reference system. Earth Planet Space 73:41. https://doi.org/10.1186/s40623-021-01370-y

Iinuma T, Ohzono M, Ohta Y, Miura S (2011) Coseismic slip distribution of the 2011 off the Pacific coast of Tohoku Earthquake (M 9.0) estimated based on GPS data-Was the asperity in Miyagi-oki ruptured? Earth Planet Space 63(7):643–648. https://doi.org/10.5047/eps.2011.06.013

Issiki H, Tsuchiya A, Kato T, Terada Y, Kakimoto H, Kinoshita M, Kanzaki M, Tanno T (2000) Precise variance detection by a single GPS receiver—PVD (point precise variance detection) method. J Geod Soc Jpn 46(4):239–251. https://doi.org/10.11366/sokuchi1954.46.239

Ito T, Yoshioka S, Miyazaki S (2000) Interplate coupling in northeast Japan deduced from inversion analysis of GPS data. Earth Planet Sci Lett 176(1):117–130. https://doi.org/10.1016/S0012-821x(99)00316-7

Kita S, Okada T, Hasegawa A, Nakajima J, Matsuzawa T (2010) Existence of interplane earthquakes and neutral stress boundary between the upper and lower planes of the double seismic zone beneath Tohoku and Hokkaido, northeastern Japan. Tectonophysics 496(1–4):68–82. https://doi.org/10.1016/j.tecto.2010.10.010

Koketsu K, Yokota Y, Nishimura N, Yagi Y, Miyazaki S, Satake K, Fujii Y, Miyake H, Sakai S, Yamanaka Y, Okada T (2011) A unified source model for the 2011 Tohoku earthquake. Earth Planet Sci Lett 310(3–4):480–487. https://doi.org/10.1016/j.epsl.2011.09.009

Langbein J, Murray JR, Snyder HA (2006) Coseismic and initial postseismic deformation from the 2004 Parkfield, California, earthquake, observed by Global Positioning System, electronic distance meter, creepmeters, and borehole strainmeters. Bull Seism Soc Am 96(4B):S304–S320. https://doi.org/10.1785/0120050823

Larson KM (2009) GPS seismology. J Geod 83(3–4):227–233. https://doi.org/10.1007/s00190-008-0233-x

Larson KM, Bodin P, Gomberg J (2003) Using 1-Hz GPS data to measure deformations caused by the Denali Fault earthquake. Science 300(5624):1421–1424. https://doi.org/10.1126/science.1084531

Larson KM, Bilich A, Axelrad P (2007) Improving the precision of high-rate GPS. J Geophys Res Solid Earth 112(B05):B05422. https://doi.org/10.1029/2006JB004367

Lichten SM, Border JS (1987) Strategies for high precision global positioning system orbit determination. J Geophys Res 92(B12):12751–12762. https://doi.org/10.1029/JB092iB12p12751

Malservisi R, Schwartz SY, Voss N, Protti M, Gonzalez V, Dixon TH, Jiang Y, Newman AV, Richardson J, Walter JI, Voyenko D (2015) Multiscale postseismic behavior on a megathrust: The 2012 Nicoya earthquake, Costa Rica. Geochem Geophys Geosyst 16(6):1848–1864. https://doi.org/10.1002/2015GC005794

Melgar D, Bock Y (2013) Near-field tsunami models with rapid earthquake source inversions from land- and ocean-based observations: the potential for forecast and warning. J Geophys Res Solid Earth 118(11):5939–5955. https://doi.org/10.1002/2013JB010506

Melgar D, Bock Y, Crowell BW (2012) Real-time centroid moment tensor determination for large earthquakes from local and regional displacement records. Geophys J Int 188(2):703–718. https://doi.org/10.1111/j.1365-246X.2011.05297.x

Melgar D, Crowell BW, Bock Y, Haase JS (2013) Rapid modeling of the 2011 Mw 9.0 Tohoku-oki earthquake with seismogeodesy. Geophys Res Lett 40(12):2963–2968. https://doi.org/10.1002/grl.50590

Minson SE, Simons M, Beck JL (2013) Bayesian inversion for finite fault earthquake source models I—theory and algorithm. Geophys J Int 194(3):1701–1726. https://doi.org/10.1093/gji/ggt180

Mitsui Y, Heki K (2013) Scaling of early afterslip velocity and possible detection of tsunami-induced subsidence by GPS measurements immediately after the 2011 Tohoku-Oki earthquake. Geophys J Int 195(1):238–248. https://doi.org/10.1093/gji/ggt256

Miyazaki S, Larson KM (2008) Coseismic and early postseismic slip for the 2003 Tokachi-oki earthquake sequence inferred from GPS data. Geophys Res Lett 35(4):L04302. https://doi.org/10.1029/2007GL032309

Miyazaki S, Larson KM, Choi K, Hikima K, Koketsu K, Bodin P, Haase J, Emore G, Yamagiwa A (2004) Modeling the rupture process of the 2003 September 25 Tokachi-Oki (Hokkaido) earthquake using 1-Hz GPS data. Geophys Res Lett 31(21):L21603. https://doi.org/10.1029/2004GL021457

Munekane H (2012) Coseismic and early postseismic slips associated with the 2011 off the Pacific coast of Tohoku Earthquake sequence: EOF analysis of GPS kinematic time series. Earth Planet Space 64(12):1077–1091. https://doi.org/10.5047/eps.2012.07.009

Niell AE (1996) Global mapping functions for the atmosphere delay at radio wavelengths. J Geophys Res 101(B2):3227–3246. https://doi.org/10.1029/95JB03048

Nishimura T, Munekane H, Yarai H (2011) The 2011 off the Pacific coast of Tohoku Earthquake and its aftershocks observed by GEONET. Earth Planet Space 63(7):631–636. https://doi.org/10.5047/eps.2011.06.025

Nishimura T, Matsuzawa T, Obara K (2013) Detection of short-term slow slip events along the Nankai Trough, southwest Japan, using GNSS data. J Geophys Res 118(6):3112–3125. https://doi.org/10.1002/jgrb.50222

Tanaka *et al. Progress in Earth and Planetary Science*   (2022) 9:55

Page 20 of 20

Nishimura T, Yokota Y, Tadokoro K, Ochi T (2018) Strain partitioning and inter-plate coupling along the northern margin of the Philippine Sea plate, estimated from Global Navigation Satellite System and Global Positioning System-Acoustic data. Geosphere 14(2):535–551. https://doi.org/10.1130/GES01529.1

Odijk D, Zhang B, Khodabandeh A, Odolinski R, Teunissen PJG (2016) On the estimability of parameters in undifferenced, uncombined GNSS network and PPP-RTK user models by means of S-system theory. J Geod 90:15–44. https://doi.org/10.1007/s00190-015-0854-9

Ohta Y, Meilano I, Sagiya T, Kimata F, Hirahara K (2006) Large surface wave of the 2004 Sumatra-Andaman earthquake captured by very long baseline kinematic analysis of 1-Hz GPS data. Earth Planet Space 58(2):153–157. https://doi.org/10.1186/BF03353372

Ohta Y, Kobayashi T, Tsushima H, Miura S, Hino R, Takasu T, Fujimoto H, Iinuma T, Tachibana K, Demachi T, Sato T, Ohzono M, Umino N (2012) Quasi real-time fault model estimation for near-field tsunami forecasting based on RTK-GPS analysis: application to the 2011 Tohoku-Oki earthquake (Mw 9.0). J Geophys Res 117(B2):B02311. https://doi.org/10.1029/2011JB008750

Ohta Y, Kobayashi T, Hino R, Demachi T, Miura S (2015) Rapid coseismic fault determination of consecutive large interpolate earthquakes: the 2011 Tohoku-Oki sequence. In: Rizos C, Willis P (eds) Proceedings of the 2013 IAG Scientific Assembly, Potsdam, Germany, vol 130. Springer, Switzerland, pp 467–475. https://doi.org/10.1007/1345_2015_109

Okada Y (1992) Internal deformation due to shear and tensile faults in a half-space. Bull Seism Soc Am 82(2):1018–1040. https://doi.org/10.1785/BSSA0820021018

Ozawa S, Murakami M, Kaidzu M, Tada T, Sagiya T, Hatanaka Y, Yarai H, Nishimura T (2002) Detection and monitoring of ongoing aseismic slip in the Tokai region, Central Japan. Science 298(5595):1009–1012. https://doi.org/10.1126/science.1076780

Ozawa S, Nishimura T, Suito H, Kobayashi T, Tobita M, Imakiire T (2011) Coseismic and postseismic slip of the 2011 magnitude-9 Tohoku-Oki earthquake. Nature 475(7356):373–376. https://doi.org/10.1038/nature10227

Perfettini H, Ampuero J-P (2008) Dynamics of a velocity strengthening fault region: implications for slow earthquakes and postseismic slip. J Geophys Res 113(B9):B09411. https://doi.org/10.1029/2007JB005398

Saastamoinen J (1972) Atmospheric correction for the troposphere and stratosphere in radio ranging satellites. Use Artif Satellites Geodesy 15:247–251. https://doi.org/10.1029/GM015p0247

Suwa Y, Miura S, Hasegawa A, Sato T, Tachibana K (2006) Interplate coupling beneath NE Japan inferred from three-dimensional displacement field. J Geophys Res 111(B4):B04402. https://doi.org/10.1029/2004JB003203

Tanaka Y, Ohta Y, Miyazaki S (2019) Real-time coseismic slip estimation via the GNSS carrier phase to fault slip approach: a case study of the 2016 Kumamoto earthquake. Geophys Res Lett 46(3):1367–1374. https://doi.org/10.1029/2018GL080741

Tsang LLH, Vergnolle M, Twardzik C, Sladen A, Nocquet J-M, Rolandone F, Agurto-Detzel H, Cavalié O, Jarrin P, Mothes P (2019) Imaging rapid early afterslip of the 2016 Pedernales earthquake. Ecuador Earth Planet Sci Lett 524:115724. https://doi.org/10.1016/j.epsl.2019.115724

Twardzik C, Vergnolle M, Sladen A, Avallone A (2019) Unravelling the contribution of early postseismic deformation using sub-daily GNSS positioning. Sci Rep 9:1775. https://doi.org/10.1038/s41598-019-39038-z

Wennerberg L, Sharp RV (1997) Bulk-friction modeling of afterslip and the modified Omori law. Tectonophysics 277(1–3):109–136. https://doi.org/10.1016/S0040-1951(97)00081-4

Yokota Y, Koketsu K, Hikima K, Miyazaki S (2009) Ability of 1-Hz GPS data to infer the source process of a medium-sized earthquake: The case of the 2008 Iwate-Miyagi Nairiku, Japan, earthquake. Geophys Res Lett 36(21):L12301. https://doi.org/10.1029/2009GL037799

Publisher's Note